UNIVERSITY OF CALIFORNIA,
IRVINE

Desalination with Charged Nanopores

THESIS

Submitted in partial satisfaction of the requirements
for the degree of

MASTER OF SCIENCE
in Physics

by
James Robert Boyd

Thesis Committee:
Professor Zuzanna Siwy, Chair
Professor Roger D. Mcwilliams
Professor Ilya Krivorotov

2018

Table of Contents

List of Figures

List of Tables

Acknowledgements

First and foremost, I would like to thank Dr. Zuzanna Siwy for allowing me the privilege of working in her lab. Under her guidance and leadership I was able to accomplish this work. Her positivity and encouragement were the single greatest factor in my success.

I would also like to thank my wife, Lesley, and son, Simon, for supporting me with love and encouragement thorough my entire education.

I also could not have succeeded without the help of all my lab mates, specifically Preston Hinkle and Crystal Yang. I wish you both the best in all your future endeavors.

Lastly, I would like to acknowledge Horizon Development, LLC., for their funding and support.

Abstract of the Thesis

Desalination with Charged Nanopores

By

James Robert Boyd

Master of Science in Physics

University of California, Irvine, 2018

Professor Zuzanna Siwy Irvine, Chair

The thesis describes development of membranes containing nanopores with charged pore walls, which could be used for desalination of brackish water. Semipermeable membranes composed of high density conical nanopore have been proposed for desalination by reverse osmosis. These nanopores feature a bipolar surface charge pattern so that the pore walls contain a junction between a zone with positive surface charges and a zone with negative surface charges. In this work we seek to show that polyimide (PI) membranes containing conical nanopores with such surface charge pattern may be produced by the process of track-etching of commercially available Kapton 50HN foils. The membranes prepared had a nanopore density of ~10^8 per cm^2. Salt rejection of the membranes was probed using 100 mM KCl as the feed solution and pressure differences up to several atmospheres. Maximum rejection of ~55% was achieved in a single-step desalination process. Modeling of salt rejection was also performed using the coupled Poisson-Nernst- Planck and Navier-Stokes equations. Our results demonstrated that conically shaped nanopores with bipolar surface charge pattern could be used for desalination of brackish water.

1. Introduction

The single most pressing problem facing humanity in the modern era may be our inability to satisfy the global demands for freshwater. Increasing worldwide population and inherent increases in the demands for agricultural products [1] and industrialization [2], already strain worldwide water availability. The unforeseeable catastrophic damage to water resources caused by natural disasters and increased impacts of climate change further imperil the availability of fresh water in all nations [3]. Even sensible strategies for water management may not be enough to provide the water we need. One alternative is to limit the freshwater withdrawals associated with agriculture and industry.

In 2016, 69% of worldwide water withdrawals were consumed by agriculture [4]. Industrial-use accounted for an additional 19%. Large scale salt-water desalination plants have been constructed in countries like Israel, China, and the United States. These plants typically produce purified water through high pressure Reverse Osmosis (RO). In recent years, improvements in membrane technology and pressure recovery have reduced the energy costs associated with large scale RO operations [5]. Plants typically operate with salt water and must be located adjacent to the ocean. Brackish water, water with salinity of about 30% of salt water salinity, is also frequently used in RO plants. Environmental cost and local accessibility still hinder freshwater procuration [6]. We believe smaller scale low-cost low pressure desalination methods will provide an answer to meet many specific challenges to worldwide water necessities.

Our current work seeks to demonstrate that nanopore membranes produced from 12 μm thick Kapton 50HN polyimide films can be optimized for maximum ionic rejection. The membranes will contain ~$10^8/cm^2$ parallel conical shaped pores and carry surface charge such that the effect length of the nanopores is in the tens of nanometers. Such membranes might be cheaply produced and used for the desalination of brackish water, opening more water resources to meet the demands of agriculture and industry.

2. Fundamentals of Ionic and Fluid Transport

Nanopores have justifiably received considerable attention over the last decade. A nanopore is a channel with nanometer dimensions. Synthetic nanopores have a variety of uses including particle sensing and counting [7] [8] [9], DNA sequencing [10] [11] and possible protein identification [12], and an ever increasing number of nanoscale electronic and fluidic devices [13]. In the present work we are particularly interested in ionic transport and selectivity in nanopores as they apply to desalination of electrolyte solutions. In this chapter we will present the physical phenomena related to ionic and fluid transport in charged nanoscale channels, including the basic equations of transport, the formation and consequences of the electrical double layer, fluid transport under pressure, reverse osmosis, ionic rejection in the presence of a bipolar junction, and simulation of ionic rejection in pores with specified geometry.

The Poisson-Nernst-Planck and Navier-Stokes equations

A basic theoretical approach for understanding fluid transport through nanopore systems begins with the derivation of the 3-dimensional generalized Poisson-Nernst-Planck (PNP) equations [14] [15] [16]. There are two physical processes which must be considered. First are those where the ionic solute moves within a static fluid. These include solute flux due to concentration gradients, electric potential gradients, and temperature gradients. Second we must consider cases where the fluid and solute moves as a whole through the nanopore, as in the case of a pressure gradient.

We will presume our experiments will take place at constant room temperature, therefore we neglect the effects of temperature gradient in the following model. First a solution of the generalized PNP for solute transport within the fluid due to a concentration gradient and an electric potential will be shown; then this solution will be modified to include the effect of a pressure gradient on the fluid.

In our nanopore system the pore length greatly exceeds the cross-sectional area allowing, in some applications, the PNP equations to be reduced to one axial-dimension along the pore [14]. In the presence of a concentration gradient within a fluid, solute in areas of high concentration will become redistributed to areas of lower concentration by diffusion. An applied electric potential gradient across the pore will create an electrophoretic flux which transports solute along or against the electric field depending on the charge sign of the ionic species.

The steady state diffusive flux of solute due to a concentration gradient may be modeled by Fick's first law in one dimension [17] as

$$j_D = -D\frac{dC\ (z,t)}{dz} \tag{1}$$

Here C is the ionic concentration and D is the diffusion constant [18]. Fick's second law eq. (2) gives the time evolution of the concentration and may be acquired by substituting eq. (1) into the continuity equation eq. (3)

$$\frac{dC\ (z,t)}{dt} = D\frac{d^2C\ (z,t)}{dz^2} \tag{2}$$

$$\frac{dC\ (z,t)}{dt} = -D\frac{dj_D\ (z,t)}{dz} \tag{3}$$

The electrophoretic flux in the presence of an electric potential gradient, eq. (4), is the product of the drift velocity of a particle and the concentration of the fluid. The drift velocity is found by applying Stoke's law eq. (5). In our system the force is due to an applied electric field, E, and is given by qE, the charge, q, of the ionic particle multiplied by the field, E. We define the viscous friction coefficient, ζ, as the ratio of the force and drift velocity. ζ is dependent upon the viscosity of the liquid and the radius of the particle. Additionally, the Einstein diffusion relation, eq. (6), provides a direct link between the viscous friction coefficient and the diffusion coefficient for mobility through a fluid by particles which obey Stoke's law.

$$j_e(z,t) = \ v_d(z,t)C(z,t) \tag{4}$$

$$v_d(z,t) = \frac{qE(z,t)}{\zeta} = \ \frac{qE(z,t)}{6\pi\eta a} \tag{5}$$

$$D = \frac{k_bT}{\zeta} \tag{6}$$

In the previous equations j_e is the electrophoretic flux, v_d is the drift velocity, η is the fluid viscosity, *a* is the particle radius, k_b is the Boltzmann constant, and T is the temperature. By substitution of (7) and (8) into (6) the electrophoretic flux becomes

$$j_e(z,t) = \ D\frac{qE(z,t)}{k_bT}C(z,t) \tag{7}$$

Noting that the electric field is defined as the negative gradient of the electric potential allows eq. (7) to be written in terms of an electric potential. Combining eq. (1) and eq. (7), the total ionic flux is

$$j_{tot}\,(z,t) = -D(\nabla C_i + \frac{z_i e C_i}{k_b T}\nabla\phi) \tag{8}$$

Eq. (8) may be applied to systems with multiple charged species by allowing i to index each ionic species, z to be the charge number of each respective species, and e the fundamental electron charge.

The Electric Double Layer

To improve upon the PNP model developed thus far we must now consider the effect of the electrical double layer on ionic and fluid transport. It will later be shown that the exposed etched surfaces of the polymer foils used in the experiment are charged when in contact with solutions of pH value greater than pH 3. This charge originates due to deprotonation of the carboxyl groups formed during the membrane fabrication process. Counterions, ions with an opposite sign to the charged surface layer, form a structure called the electric double layer [20] [21], which consists of a thin layer of immobile counterions close to the surface (Stern Layer), and a diffuse layer, in which the counterions are free to move (Figure 2.1). The presence of the electric double layer adds important implications to our understanding of fluid transport through a charged nanopore.

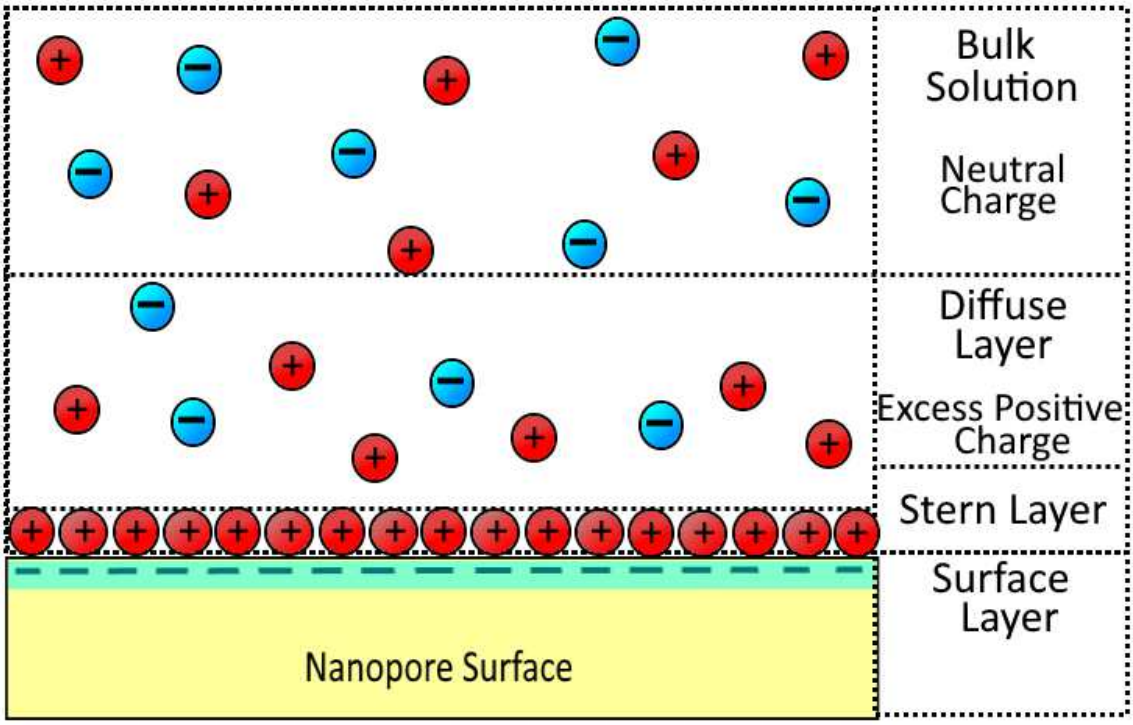

Figure 2.1. **The Electric Double-Layer at a charged interface**. At the surface of a charged interface a layer of immobile counter-ions forms (the Stern Layer). Adjacent to the stern layer the solution has an excess concentration of counterions (the diffuse layer).

In the diffuse layer our system may be modeled by considering a charged particle in a large volume of electrolyte solution bound by an infinite charged plate. The solution of such a system is described by the well-known Poisson-Boltzmann (PB) equation.

We now derive the PB equation, starting with an alternate form of Poisson's equation where the charge density ρ is given in terms of concentration [17]

$$\nabla^2\phi(x,t) = \frac{-\rho}{\varepsilon_0} = \sum_c \frac{FzC(x,t)}{\varepsilon} \tag{9}$$

Here ϕ is the potential, F is the Faraday constant, C is the concentration of each species of the electrolyte solution, z is the valence number of each species, and ε is the permittivity of the solution. In the solution, the concentration of the free ions are described by a Boltzmann distribution.

$$C_+(x,t) = C_0 e^{\frac{-Fz\phi(x,t)}{RT}} \tag{10}$$

$$C_-(x,t) = C_0 e^{\frac{Fz\phi(x,t)}{RT}} \tag{11}$$

We use the Faraday constant since we desire the Molar concentration of the solution. After substituting equations eq. (10) and eq. (11) into eq. (9), and using the small angle approximation for hyperbolic sin, valid for small surface potentials

$$\rho(x,t) = zFC_0(e^{\frac{-Fz\phi(x,t)}{RT}} - e^{\frac{Fz\phi(x,t)}{RT}}) = -2zFC_0 \sinh\left(\frac{Fz\phi(x,t)}{RT}\right) \tag{12}$$

$$\rho(x,t) = -\left[\frac{2F^2z^2}{\varepsilon RT}\right]\phi(x,t) = -\frac{\phi(x,t)}{\lambda_D} \tag{13}$$

Eq. (9) may now be solved for the potential in the low potential regime. The boundary conditions for this regime include matching the potential at the surface at x=0 and allowing the potential to be 0 when x becomes very large. In the low potential regime $Fz\phi(x,t) \ll k_bT$, satisfied at room temperatures for which $Fz\phi(x,t)$ is significantly less than 25 meV; the solution shows the Debye potential decreases as [21]

$$\phi(x,t) = \phi_{surf} e^{-\frac{x}{\lambda_D}} \tag{14}$$

The leading term in eq. (13) must have units of m^{-2}. This term eq. (15) is the characteristic length scale which governs behavior of ions in electrolyte solutions near a charged surface and is known as the Debye length.

$$\lambda_D = \left(\frac{\varepsilon RT}{2F^2 z^2 C_0}\right)^{\frac{1}{2}} \tag{15}$$

The Debye length is critically dependent on the concentration of the electrolyte solution and a crucial component of the physical mechanisms which enable nano-size pores to exhibit many useful ion transport phenomena not generally seen in macroscopic systems. In KCl at 1 M concentration the Debye length is 0.3 nm. In macro-size pores the ratio of the Debye length to the overall diameter of the pore is negligible.

Ion Transport Under the External Applied Pressure Difference

We must examine the case when fluid flow through our nanopores is driven by an external pressure source. The generalized continuity equation for the flux and divergence of the mass density of a system subject to an external pressure is

$$\frac{d\rho}{dt} + \nabla \cdot (\rho \boldsymbol{v}) = 0 \tag{16}$$

For incompressible fluids which may be modeled as Newtonian fluids the Navier-Stokes equation of the momentum of the system can be written as [23]

$$\rho \left(\frac{dv}{dt} + \boldsymbol{v} \cdot \nabla \boldsymbol{v}\right) = -\nabla p + \mu \nabla^2 \boldsymbol{v} + f \tag{17}$$

The final term in eq. (17) is a body force term, identified with electroosmotic flow, due to the applied potential. Eq. (17) demands modification of eq. (8) to include pressure. Looking forward to the next section, we also include a hinderance factor, K, as proscribed by the more complete transport equations derived by [22], [24]

$$j_{tot}\,(z,t) = -K_{i,d}D\left(\nabla C_i + \frac{z_i e C_i}{k_b T}\nabla\phi\right) + K_{i,c}C_i v \qquad (18)$$

These equations allow us a description of the transport of ionic species (in fluid) through a nanopore with conical geometry.

Volumetric Flow Rate and the Hagen-Poiseuille Equation

The geometry of a single conical nanopore is shown in Figure 2.2. Characterization of the physical parameters of a single conical nanopore is carried out by using the simple approximation for a conical resistor [25].

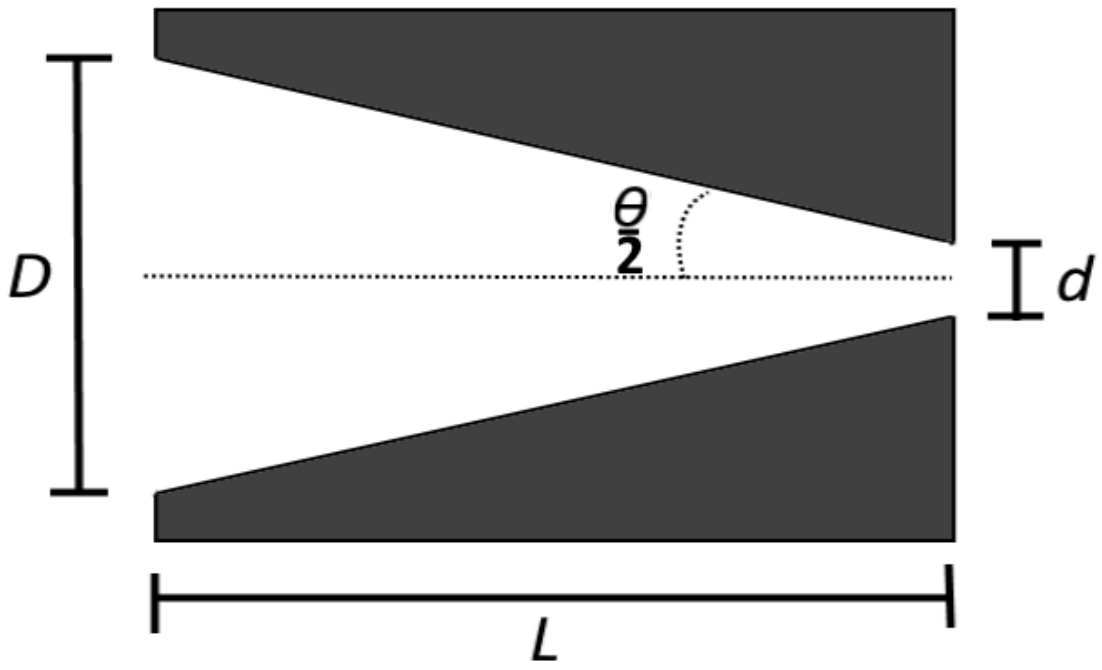

Figure 2.2. Geometric Characteristics of a Conical Nanopore. The geometry of a conical nanopore is shown. Here d is the size of the tip diameter, L is the width of the material, D is the estimated diameter of the base, and θ/2 is the half-open angle.

The tip diameter, d, of a single conical nanopore may be computed from eq. (19). It is determined from the bulk material etch rate, D, the thickness (length) and conductivity, κ, of the material, and conductance, I/V, of the nanopore measured by current-voltage curve.

$$d = \frac{4LI}{\kappa\pi DV} \tag{19}$$

Siwy, et al [26], found Kapton 50HN has a bulk material etch rate of 444 nm/hour. Current-voltage curves are measured by placing the nanopore between two conductivity cells and applying a sweeping voltage from negative to positive 1 V. The conductivity

cells are filled with 1 M KCl to minimize the effect of the electric double layer on ionic transport. Measurement of the resultant current is done by AG/AGCl electrodes.

This simple approximation scheme works well for characterizing single nanopores, but not for multipores. A second method for approximating the physical parameters of the multipore membranes utilizes the Hagen-Poiseulle (HP) equation for laminar, viscous flow of incompressible Newtonian fluid [21],

$$Q = \frac{\pi \Delta p}{8 \mu L} R^4 \tag{20}$$

Here Q is the volumetric flow rate, Δp is the pressure gradient, μ is the dynamic viscosity of the electrolyte, L is the thickness of the membrane, and r is the diameter of the pore respectively.

Eq. (21) is derived from the momentum equation, eq.(17), under the assumption that the flow rate is maximum at the center of the pore and that there is a no slip condition along the interior pore surfaces [21].

$$\nabla^2 v = \nabla p + F(z_+ C_+ + z_- C_-) \nabla \phi \tag{21}$$

With

$$C_{\pm} = C_0 \exp\left(\mp \frac{zF\zeta}{RT}\right) \tag{22}$$

Additionally, we assume overall charge neutrality within the pore and equivalence of the concentration for each ionic species. Dividing the total flow by the total number of pores gives the average flow rate per pore, shown to be

$$\frac{Q}{N} = \frac{\pi}{8N\mu L} R^4 \left(p - 2zFC_0 \sinh\left(\frac{zF\zeta}{RT}\right)\right) \quad (23)$$

If C_+ and C_- equal the initial concentration, C_0, then the argument of the exponential term in eq. (22) and the argument of the hyperbolic sine term in eq. (23) are both zero. Eq. (23) necessarily reduces to eq. (20).

For a narrow conical pore, we may approximate the pore diameter by the average of the tip and base diameter, expand this average as a series, and drop terms of higher order than r^2R^2 [am].

$$\frac{Q}{N} = \frac{\pi \Delta p}{8\mu L} r^2 R^2 \quad (24)$$

Surprisingly, although this equation has been extremely simplified it provides order of magnitude approximations of the tip diameter as confirmed by measurement of tips successfully imaged by Scanning Electron Microscopy.

Further Considerations (Osmotic pressure, Donnan potentials, steric rejection)

Two final phenomena which need to be considered for desalination are osmotic pressure and Donnan potentials. When two volumes of solvent, initially at different ionic concentrations, are placed on either side of a membrane impermeable to the ions, water will diffuse from the solvent at lower chemical potential to the solvent of higher concentration until either the chemical potential of each solvent is equal or hydrostatic pressure neutralizes further flow. This is the well-known osmotic pressure [28], often designated as Π.

$$\Pi = iCRT \tag{25}$$

Here C is the concentration of the fluid, R is the ideal gas constant, T is the temperature, and i is the van't Hoff factor [28], the ratio between the concentration of the ionic species when dissolved and in the initial mass. For electrolyte fluids with two species of ions the van't Hoff factor is near 2.

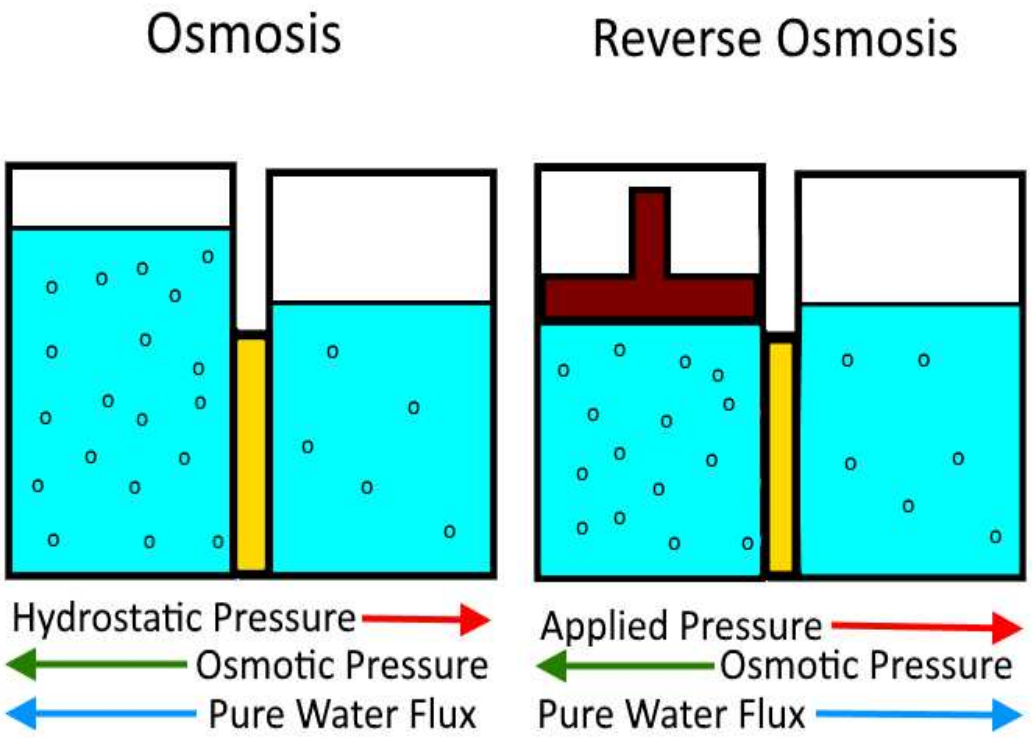

Figure 2.3. Osmosis and Reverse Osmosis systems. Osmosis (left) occurs when solvent moves towards a more concentrated solution through a semipermeable membrane that allows only the solvent to pass through. Reverse Osmosis (right) occurs when applied pressure drives solvent across a semipermeable membrane against osmotic pressure.

Reverse Osmosis systems use pressure to drive water against the chemical potential gradient, effectively reversing the process and pushing pure water from the high concentration solution to the lower concentration. Osmosis and reverse osmosis are shown in Figure 2.3. For fluids driven by external pressure through a semipermeable membrane, the solute flux *j,* depends on the difference between the applied pressure gradient Δp and the osmotic pressure gradient $\Delta \Pi$, multiplied by a permeability factor A. The permeability of particular membranes may vary based upon the temperature and pH of the solution. The flux can be written as [27] [28]

$$j = A(\Delta p - \Delta \Pi) \tag{26}$$

The permeability factor is inversely related to a solute rejection coefficient, R_s, which is a function determined by the physical system we hope to describe by coupled PNP and NS equations.

At the boundaries of the pore, where there is a concentration gradient, specifically in our case at the base and tip, a potential forms which acts to impede the flow of ions from regions of higher concentration to regions of reduced concentration in order to maintain electro-neutrality. Within the confines of the nanopore, in particular due to the electric double layer, the concentration of counterions will be greater than the concentration outside the nanopore. This boundary potential is known as a Donnan Potential.

Finally, we must consider steric rejection. As mentioned previously, when considering solutes with ionic concentrations of 1M or less, the Debye layer of our nanopores is approximately 0.3-1 nm or more. Later we shall show our pores may have tip diameters of at least several nanometers. Thus, steric rejection alone, even when considering ionic solvation, is unlikely. Ionic solvation happens when water molecules electrostatically attracted to the ion, form shells around the ion increasing its effective diameter to 5 nm or more [29] [30]. However, for the sake of completeness, steric rejection must also be accounted for in any plausible theory of ionic rejection by charged nanopores.

Szymczyk, Zhu, and Balannec [22], derive a more complete model of salt rejection for cylindrical nanopores with low surface charge densities or in the case where the Debye length is greater than the pore radius. Again the length of the nanopore is much greater than the opening radius and all variables take on their radially averaged values so that the 3-D NP equations reduce to 1-D. Under these conditions eq. (18) is rearranged and becomes

$$\frac{dc_i(z,t)}{dz} = \frac{J_v}{K_{i,d}D_i}\left(K_{i,c}C_i(z) - C(p) - \frac{z_i e C_i(z)}{k_b T}\nabla\phi(z)\right) \tag{27}$$

In eq. (27) all values should be considered radially averaged quantities. C(p) is the concentration outside the tip of the nanopore, J_v is the fluid velocity. The radially averaged electric field may be derived from eq. (27) by requiring local electro-neutrality within the pore

$$\sum z_i C_i = X_i = \frac{2\sigma(z)}{Fr} \tag{28}$$

where σ(z) is the surface charge density and r is the pore radius. The radially averaged electric field is found by substituting eq. (28) into eq. (27) and solving eq. (29)

$$E(z) = -\frac{d\phi(z)}{dz} \tag{29}$$

The result is

$$E(z) = \frac{RT}{F c_i z_i^2}\left[\frac{J_v}{K_{i,d} D_i}\left(K_{i,c} C_i(z) - C(p)\right) - \frac{dX(z)}{dz}\right] \tag{30}$$

There is an osmotic pressure jump at both the entrance and exit of the pore. Denoting the concentration outside the pore on the side where pressure is applied C(f) and the opposite exterior region C(p), the total osmotic pressure jump is given as

$$\Delta P_o = RT \sum \big(C(f) - c_i(f)\big) + \left(c_i(p) - C(p)\right) \tag{31}$$

Again, the summation is over the i ions and c(f) and c(p) represent the concentration inside the pore at the entrance and exit, while C(f) and C(p) represents the bulk concentration outside the pore at the entrance and exit. Finally the total pressure across the pore is given by adding eq. (31) to Stoke's equation

$$\Delta P = \frac{8\eta L}{R^2} J_v + F \int_{z=p}^{z=f} X(z) \frac{d\phi}{dz} dz + \Delta P_0 \tag{32}$$

The boundary conditions necessary to solve eqs. (27), (30) and (32) are given by the solute concentration inside the pore at the entrance and exit. These may be formulated as follows, incorporating a term for steric rejection, δ, and the Donnan potential at each boundary ψ [22]

$$c_f = C_i(f)\delta \exp(-z_i \Delta\psi_b) \tag{33}$$

$$c_p = C_i(p)\delta \exp(-z_i \Delta\psi_t) \tag{34}$$

Finally, the rejection rate, R, of a nanopore is determined by the weighted difference of the feed and permeate concentrations

$$R = \frac{c_f - c_p}{c_f} \tag{35}$$

Modification of Surface Charge to Create Bipolar Junctions

Electrostatic rejection by nanopores may be improved by chemical modification of the pore walls to create two separate oppositely charged regions along the surface of the nanopore (Figure 2.4) [22] [31] [32] [33]. The boundary between the two regions forms a space charge region where concentrations of both cations and anions are depleted.

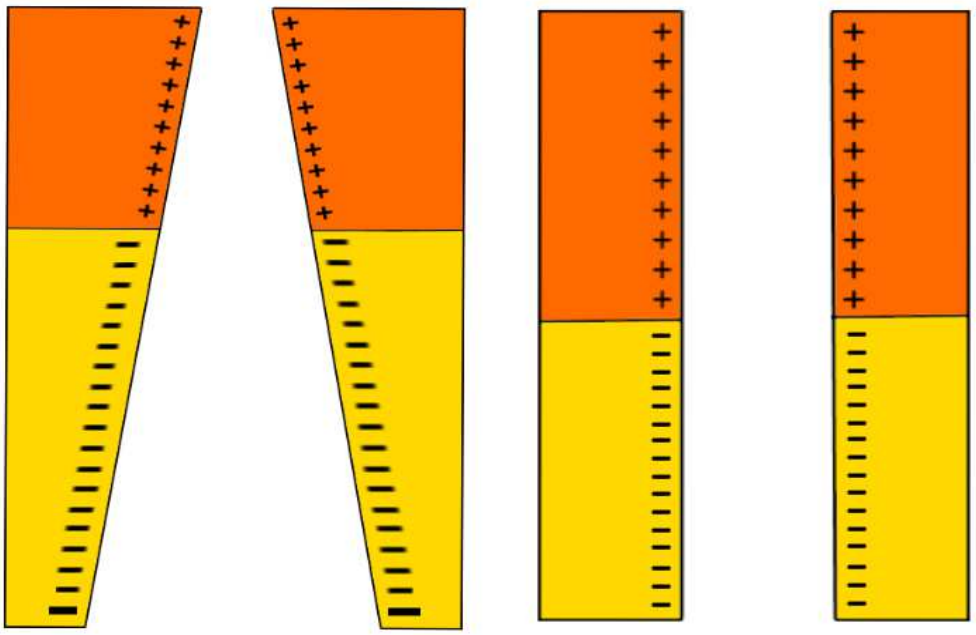

Figure 2.4. Patterned Surface Charge for Two Nanopore Geometries. An example of asymmetric patterned surface charge regions for a conical (left) and cylindrical (right) nanopore. The region with the junction between zones with positive and negative surface charges creates aspace charge region, where the concentrations of both ions are depleted.

The depletion zone forms an additional boundary to the passage of solute through the pore. Figure 2.5 provides a schematic example of ionic flow and selectivity through a cylindrical pore with asymmetric patterned surface charge.

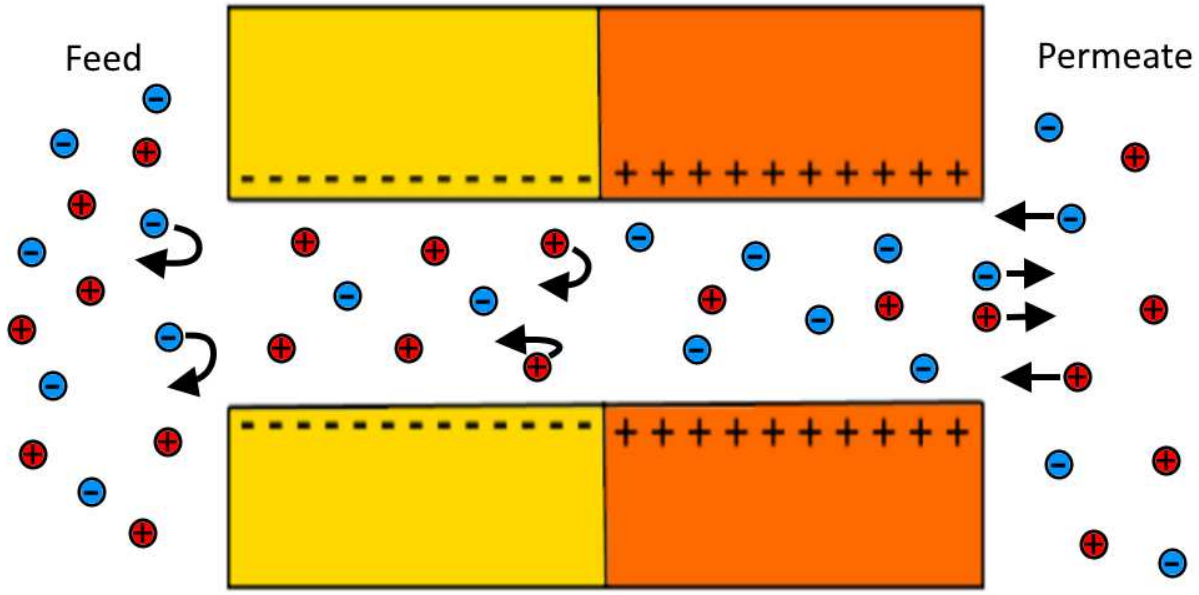

Figure 2.5. Ionic Flow thru a Cylindrical Nanopore with Patterned Surface Charge. A Donnan type potential at each boundary hinders ions of similar charge sign to each adjacent surface. Additionally chargeneutrality within the pore demands replacement of ions which exit the pore by ions primarily sourced either from the feed or permeate solutions.

When a pressure gradient is applied at the entrance of the nanopore, ions which carry identical charge sign to the first charged region experience a Donnan like potential which acts to selectively reject only these ions. The Donnan potential arises because diffusion out of the entrance of the pore is more energetically favorable then passage into the next charged region. Similarly, ions of the same charge sign may enter the first charged region but are repelled at the depletion zone. Again diffusion into the first charged region is energetically favorable to crossing the depletion zone and entering the second charged region. The interior of the pore also must maintain charge neutrality. As such, ionic species which successfully exit the pore must do so in cation-

anion pairs. In order to maintain electroneutrality within the pore, ions in the second charged region are preferentially replaced from the permeate solution over those in the first charged region. Salt rejection may also be improved by optimizing the length of the second charged region.

Patterned charge modification of the nanopores in this experiment was performed with spermine coupled by 1-ethyl-3-[3(dimethylamino)propyl] carbodiimide hydrochloride (EDC) to the surface carboxyl groups exposed during the etching process. Modification was confirmed by observation of rectification reversal of a current-voltage curve. The magnitude of the current and rectification ratio were generally found to be reduced after modification, suggesting spermine did not successfully couple to all of the carboxyl groups in the positive charge region [26]. Figure 2.6 shows a current-voltage curve of a Kapton membrane before and after modification by 80 min exposure to EDC with spermine at the tip side of the membrane.

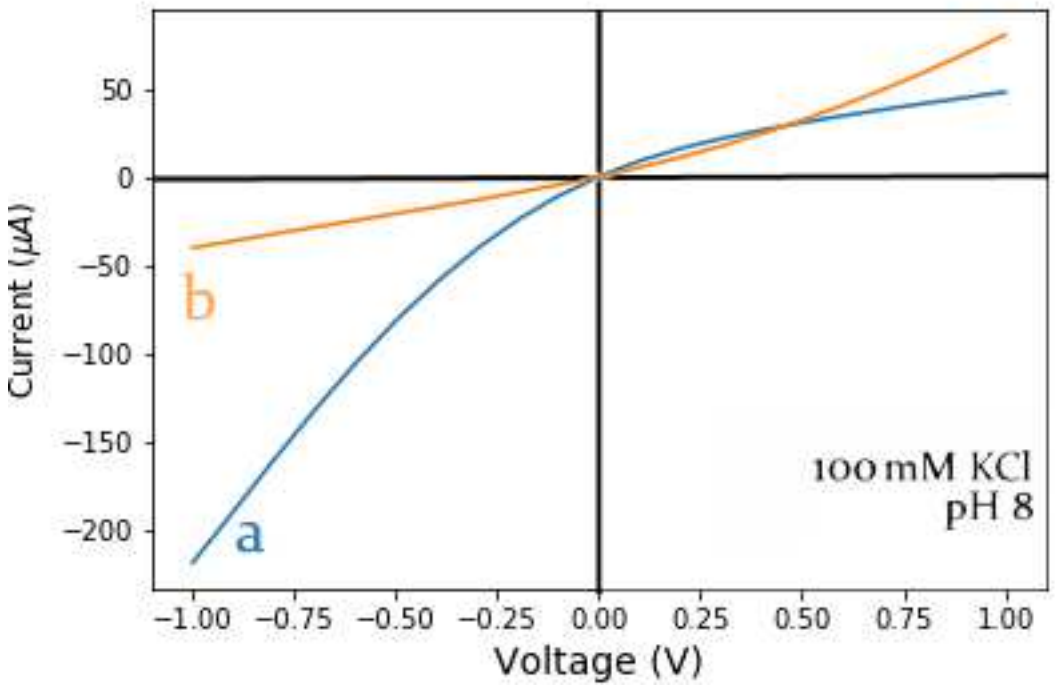

Figure 2.6. Rectification of a Modified Kapton Membrane. A Kapton membrane before (blue 'a') and after (orange 'b') 80 minute modification by 50 mM EDC and 50 mM spermine. Note Rectification curve reverses after modification. Reduction of current and rectification ratio after modification is believed due to incomplete carboxyl-spermine coupling due to short modification time.

Simulation Data for Cylindrical and Conical Nanopores

In order to simulate the flow and rejection capabilities of our nanopores, numerical solutions of the PNP-NS equations were found using Comsol Multiphysics 4.4 for the two pore geometries shown in Figure 2.7. The cylindrical nanopore has a length of 1 μm and an opening diameter of 10 nm. The conical pores have a length of 11 microns and varied tip and base diameters. The upper compartment *ABCD* contains pure solvent, while the pore and lower compartment *FGHI* contain the concentrated solution. Pressure was driven across the pore from base to tip.

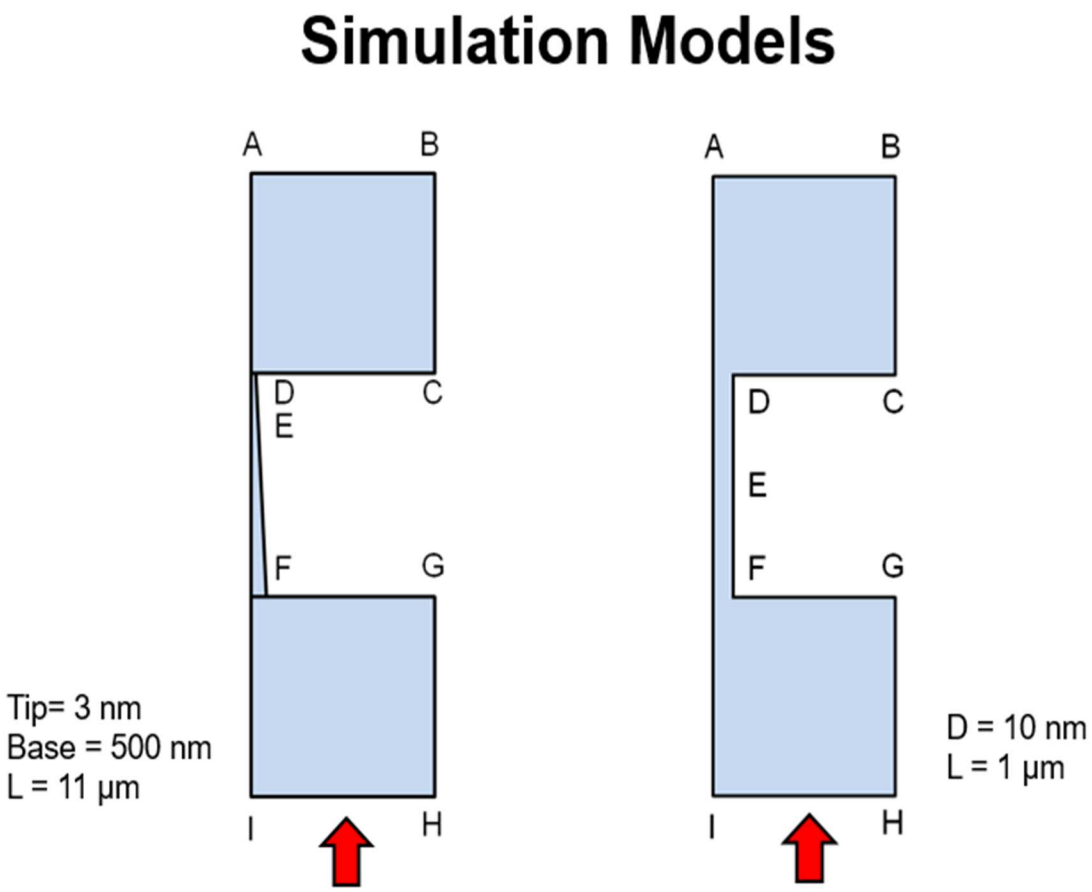

Figure 2.7. Model of Nanopores Considered in Numerical Modeling. The conical pore (left) has openings of 3 nm at the tip and 500 nm at the base; pore length was 11µm. A range of tip and base diameters was also considered. The cylindrical pore (right) has a 10 nm diameter with pore length of 1 µm.

We first analyzed salt rejection offered by a cylindrically shaped nanopore [26]. We considered a pore with an opening of 10 nm in diameter because the model for narrower pores and a length of 1 µm did not converge. One portion of a pore had positive surface charges and the other portion negative surface charges, creating a bipolar surface charge pattern as shown in Figure 2.8.

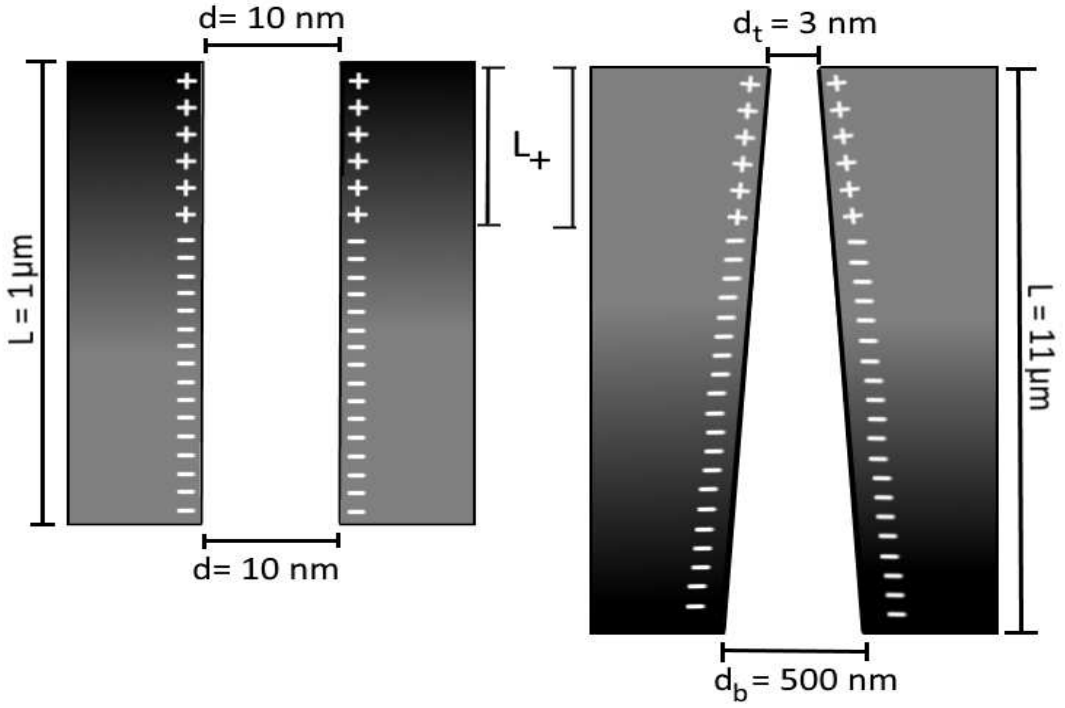

Figure 2.8. Cylindrical and Conical Nanopore with Bipolar Charge Zone. A scheme of a cylindrical nanopore (left) and conical nanopore (right) used in the modeling of salt rejection. Note the bipolar surface charge pattern; thus there exists a junction between positively and negatively charged zones.

Figure 2.9 presents the predicted salt rejection of the cylindrical nanopore shown in Figure 2.8 as a function of increasing surface charge density in both the positive and negative zones of the pore for three different values of feed concentration. The rejection ratio is calculated as the ratio of the concentration of permeate and feed solutions [22], respectively. Note that although the pore opening is 10 nm, thus several times greater than the Debye length, the rejection ratio was predicted to reach even 80% in feed concentration as high as 100 mM KCl when the surface charge density increased to 0.4 C/m^2.

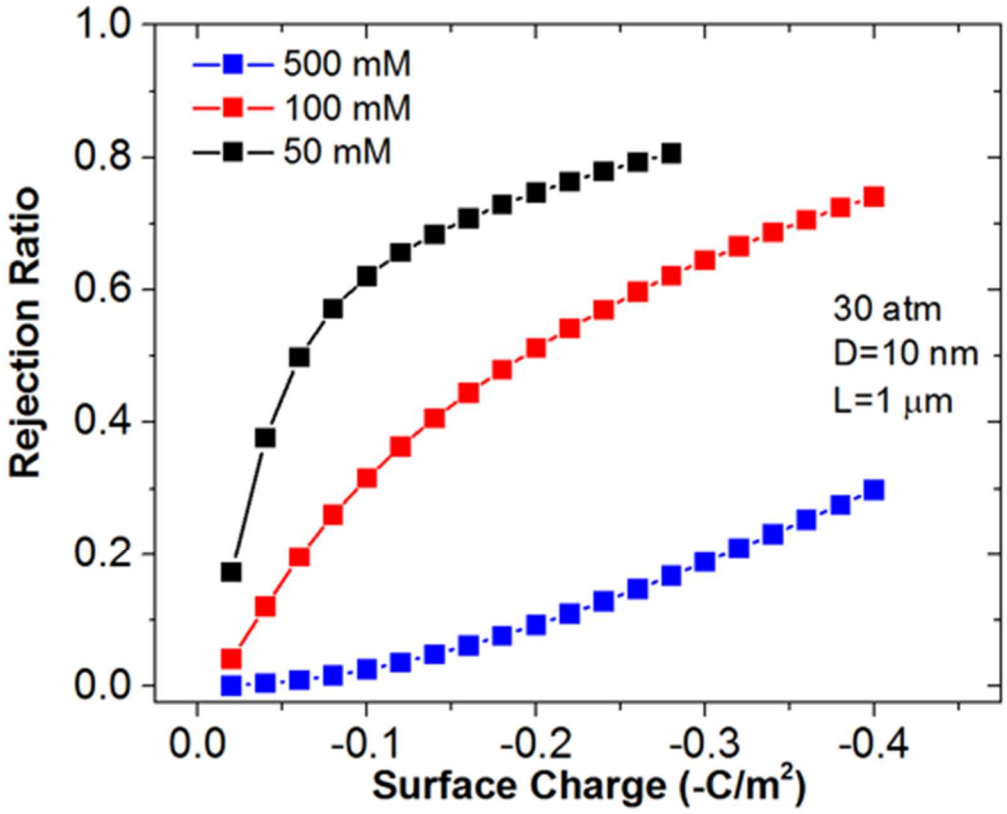

Figure 2.9 Salt Rejection by a Cylindrical Nanopore. Predicted salt rejection ratio for a 10 nm diameter cylindrical nanopore with diode surface charge pattern as shown in Figure 3.2.

Salt rejection performance of cylindrical pores as a function of feed salt concentration was investigated as well. As expected, as the salt concentration in the feed decreases, the salt rejection is improved. The modeling was performed for a cylindrical nanopore with charge zones having surface charge density of 0.08 C/m^2.

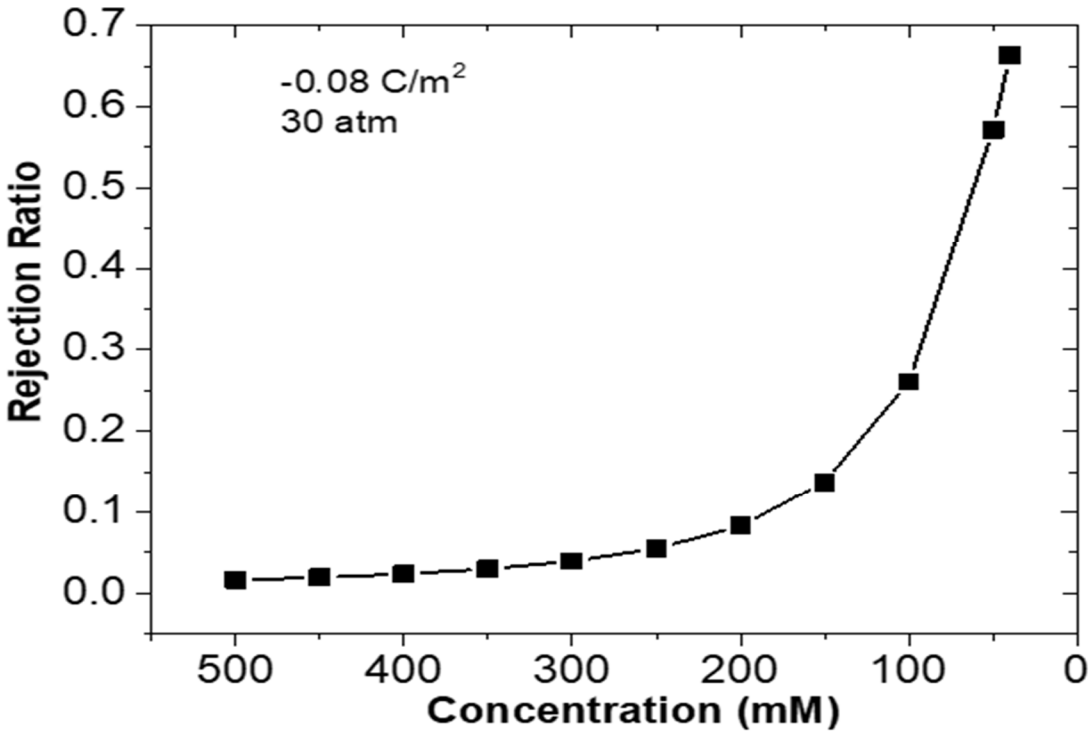

Figure 2.10. Concentration Dependence of Desalination for a Cylindrical Nanopore. Desalination of a cylindrical nanopore as a function of the concentration of the feed solution is shown. Pores were modeled as shown in figure 3.2 with surface charge density of 0.8 C/m^2.

Finally we looked at the rejection ratio of cylindrical nanopores as a function of pressure difference and pore length, Figure 2.11 and Figure 2.12. Increasing both parameters leads to improved desalination performance, until a saturation is observed. The pressure difference dependence could be explained by considering the Peclet number, which is defined as the product of the volume flux and pore length divided by the diffusion constant of the solute [36] [37]. Peclet number indicates the ratio of advective (pressure driven in our case) transport to the diffusive transport rate. For high fluxes and high Peclet numbers, the charge density at the entrances of the pores govern rejection. The effect of the pore length could be understood by considering the area of interactions between the passing ions and the pore walls. Longer pores have larger area of interactions, which can facilitate salt rejection.

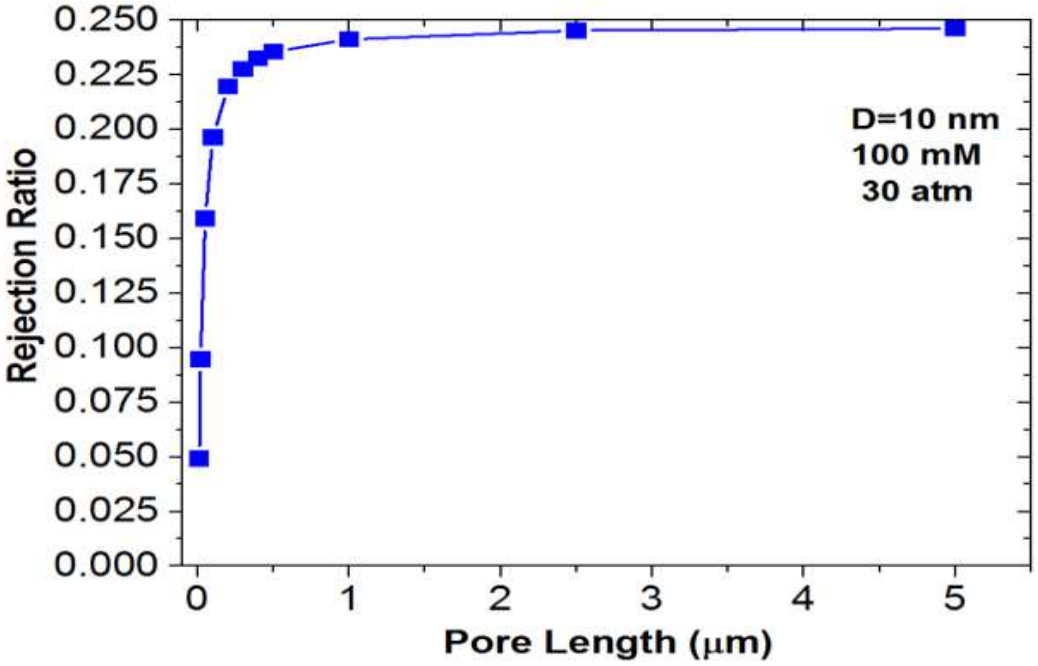

Figure 2.11. Salt Rejection of a Cylindrical pore as a Function of Pore Length. Rejection is shown for a feed solution of 100 mM KCl at 30 atm.

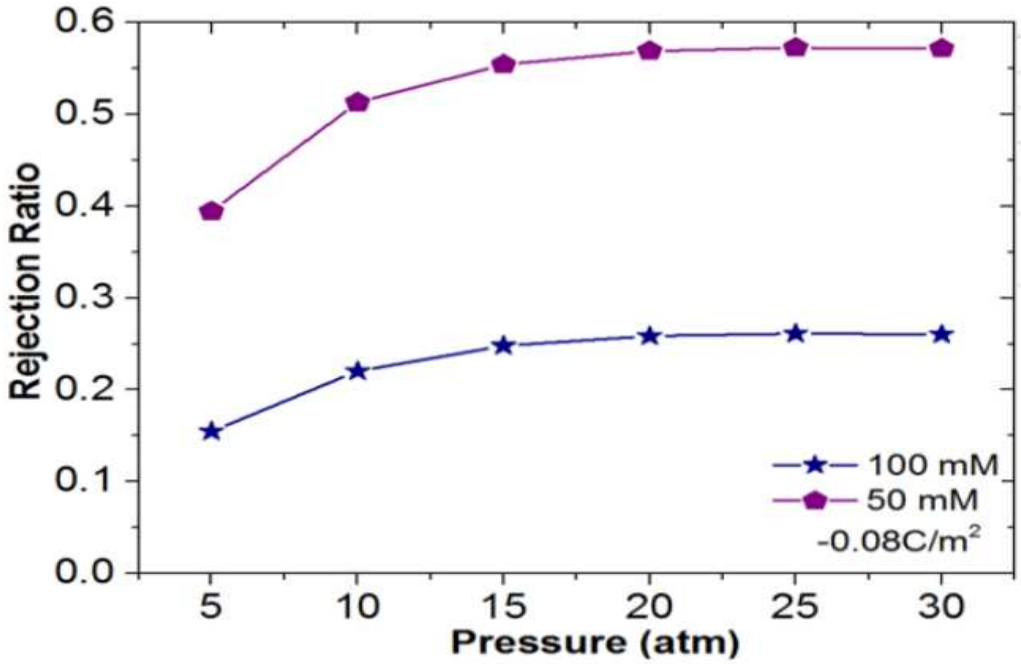

Figure 2.12. Salt Rejection of a Cylindrical pore as a Function of Pressure. Salt rejection of a 1 μm long cylindrical nanopore with 10 nm diameter openings as a function of pressure is shown for two concentrations, 50 mM and 100 mM KCl.

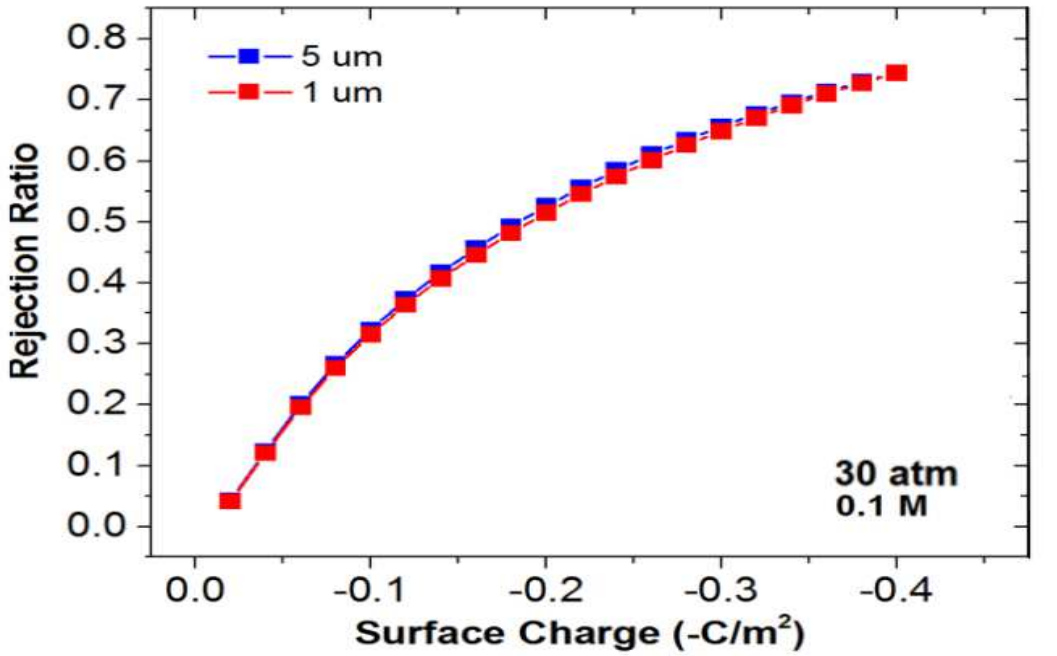

Figure 2.13. Rejection Dependence on Surface Charge Density for a Cylindrical Nanopore. Rejection ratio versus surface charge is shown for cylindrical nanopores having two different lengths. Rejection shown is for 100 mM concentration at 30 atm through a 10 nm diameter cylindrical nanopore.

Figure 2.13 supports the result obtained in figure 2.11; that, indeed, once the pore length reaches 1 μm, the rejection is not improved with further pore length increase.

As the next step, we modeled salt rejection performance of conically shaped nanopores. The number of parameters one could consider in this case is much higher. This is because salt rejection could depend not only on the length of the positively charged zone and pressure, but also tip opening diameter and cone opening angle,.

First we considered a nanopore with a tip opening of 3 nm and base diameter of 500 nm. Figure 2.14 shows desalination by such a pore when we vary the length of the

positively charged zone located at the tip, L_+. For L_+ up to ~25 nm salt rejection is maintained nearly at the same level and then steeply decreased as positive zone length increased. This result may be understood by taking into account the gradually increasing local diameter as we move away from the tip. When the transition zone between positive and negative surface charges is located in a region where the local diameter is too large to become ion selective, the pore functions as if the entire pore length was overall positively charged.

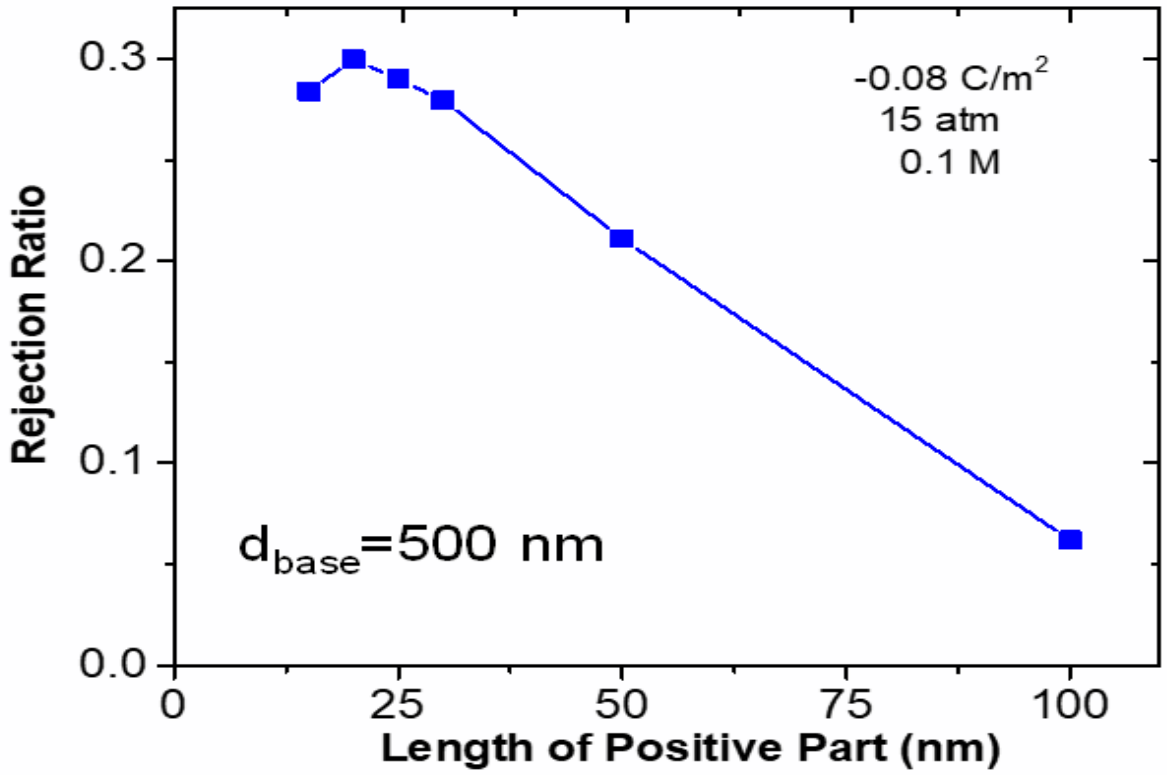

Figure 2.14 Salt Rejection by a Conical Nanopore with Bipolar Surface Charge Densities. Salt rejection thru a nanopore with 3 nm tip and 500 nm base diameters and bipolar surface charge zones is shown. The surface charge density for both the positive and negative zones is 0.08 C/m^2.

The same conically shaped nanopore was also probed as a function of feed KCl concentration. Figure 2.15 shows rejection ratio increases with decreasing feed concentration. This result was similarly found for cylindrical pores in figure 2.10.

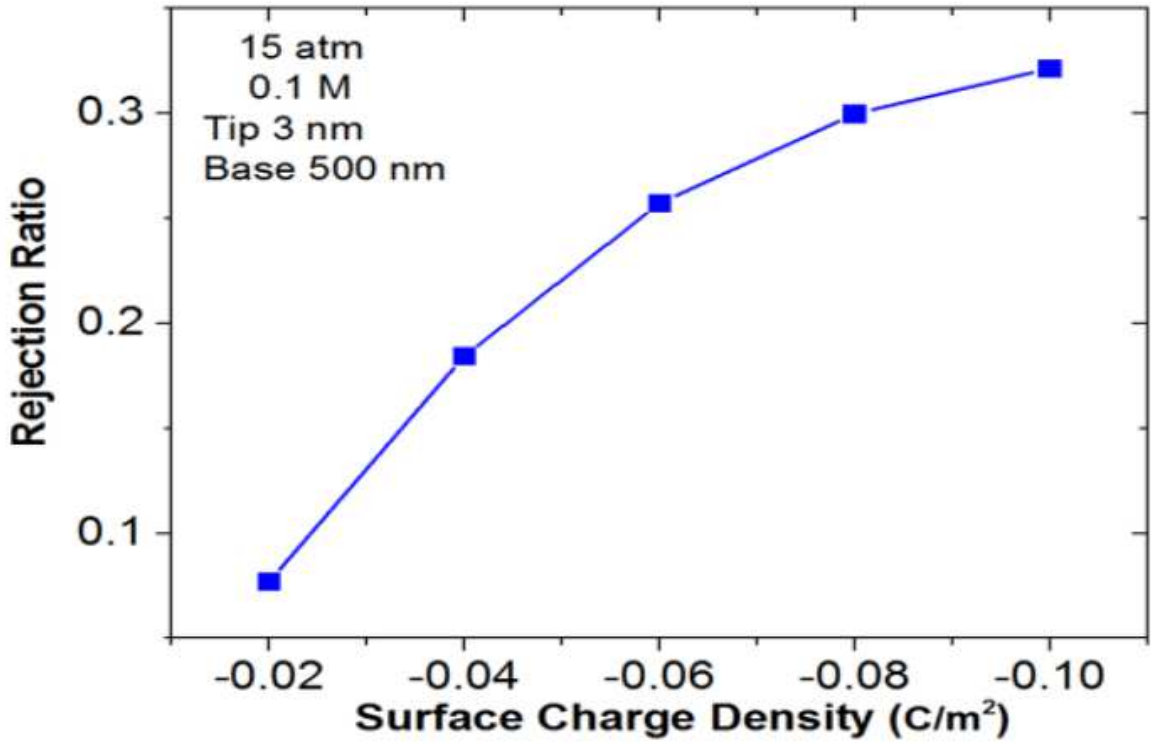

Figure 2.15. Rejection Dependence on Surface Charge Density for a Conical Nanopore Rejection ratio versus surface charge density for a canonical nanopore with 3 nm tip and 500 nm base diameters and bipolar surface charge zones is shown. Rejection is shown for 100 mM KCl feed at 15 atm.

The influence of the geometrical parameters of the conical nanopore on desalination was also probed as shown in figure 2.16 and figure 2.17. First, the tip diameter was changed between 2 nm and 15 nm, while keeping the base diameter at 500 nm. Then the base opening was changed between 250 nm and 1 μm, while keeping the tip diameter at 3 nm. Both sets of modeling suggested there as an optimal

range of cone opening angles for which the desalination was the highest. As expected the desalination is strongly dependent on the tip opening diameter.

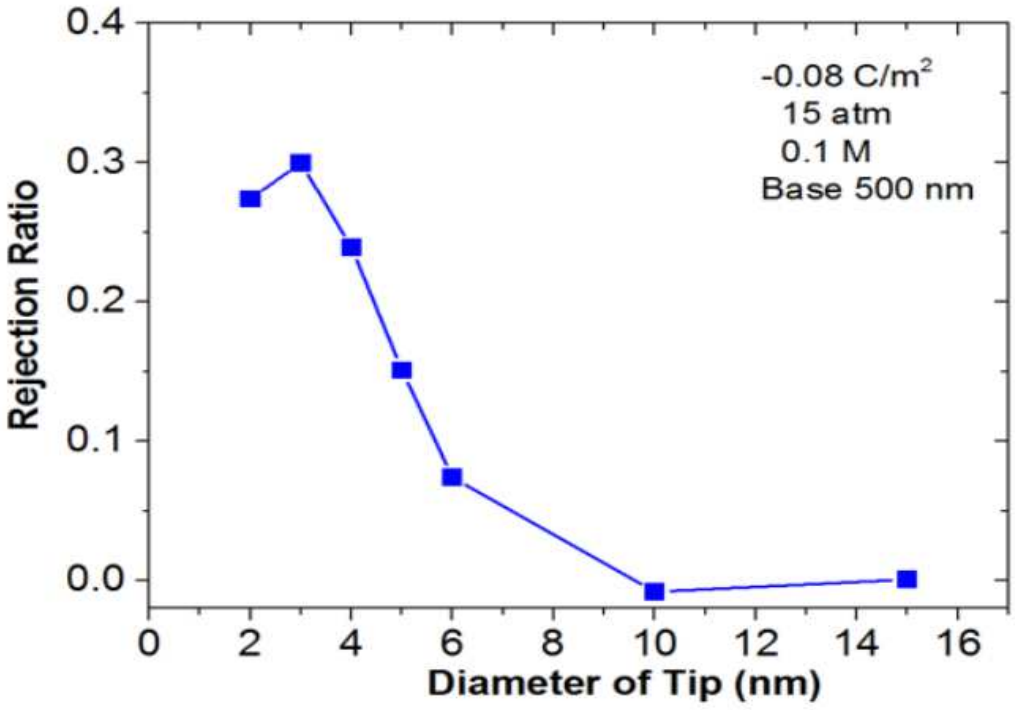

Figure 2.16. **Rejection Ratio Dependence on Tip Diameter for a Conical Nanopore**. Desalination of a conical nanopore with 500 nm base diameter opening and tip diameter varied between 2 nm and 15 nm.

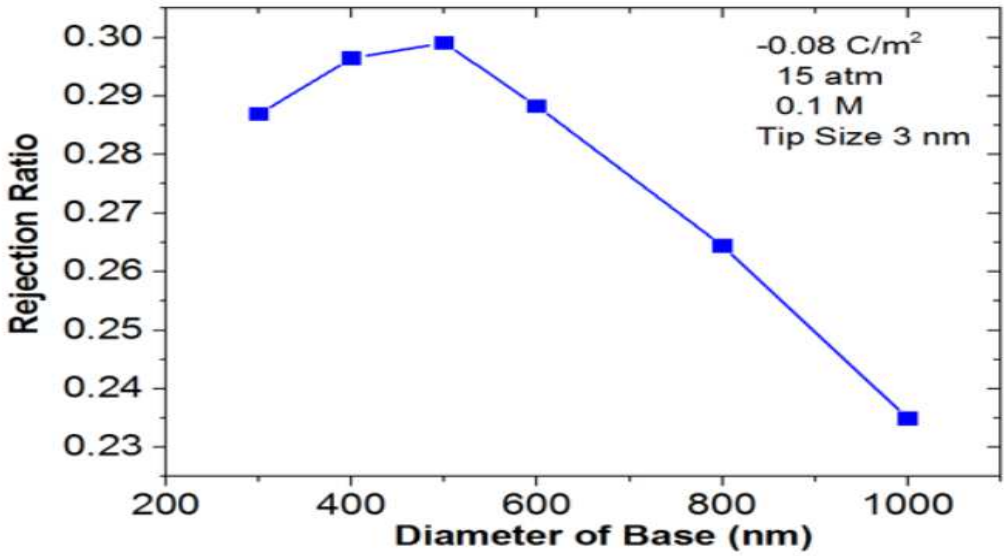

Figure 2.17. Rejection Ratio Dependence on Base Diameter for a Conical Nanopore. Desalination of a conical nanopore with 3 nm tip diameter opening and base diameter varied between 300 nm and 1000 nm.

Finally, we consider the effect of increased pressure on desalination through a conical nanopore. Figure 2.18 salt rejection initially increases with increasing pressure before reaching saturation at ~30 atm. A similar result was observed for cylindrical pores in figure 2.12.

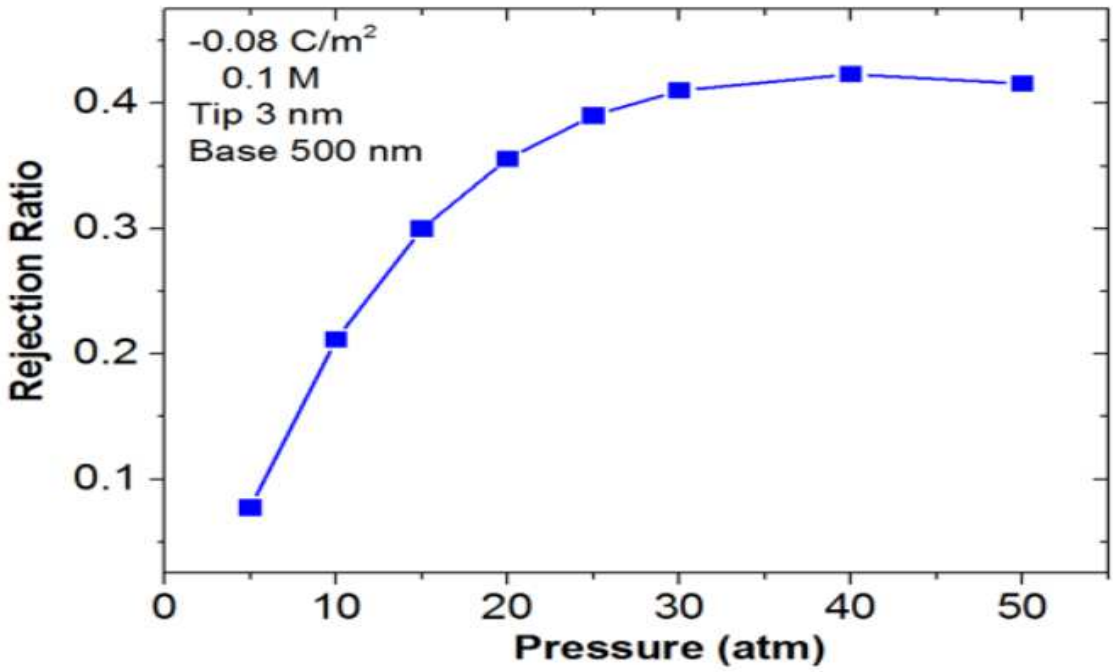

Figure 2.18. Rejection Ratio Dependence on Pressure for a Conical Nanopore. Rejection ratio versus pressure for a conical nanopore with 3 nm tip and 500 nm base diameters is shown. Rejection shown is for 100 mM KCl feed concentration at pressure varied from 5 atm to 50 atm.

The interplay of all geometric effects is shown in Figure 2.19. Different lengths of the positively charged region, L_+, and opening diameters of tip and base are considered. The results confirm our earlier conclusion that the area of interactions between the passing ions and the pore walls influences desalination: pores with smaller opening diameter exhibit larger rejection ratios. In addition, salt rejection is also strongly dependent on the position of the junction between positively and negatively charged regions. Specifically, if the L_+ is just a few nm long, none of the considered conical pores exhibited significant desalination. For a pore with the tip of 2 nm and base of 500 nm, desalination can be achieved with L_+ <50 nm; for the less conical pore with the base opening of 250 nm, the pore can desalinate in a wider range of L_+ values, up to 60 nm.

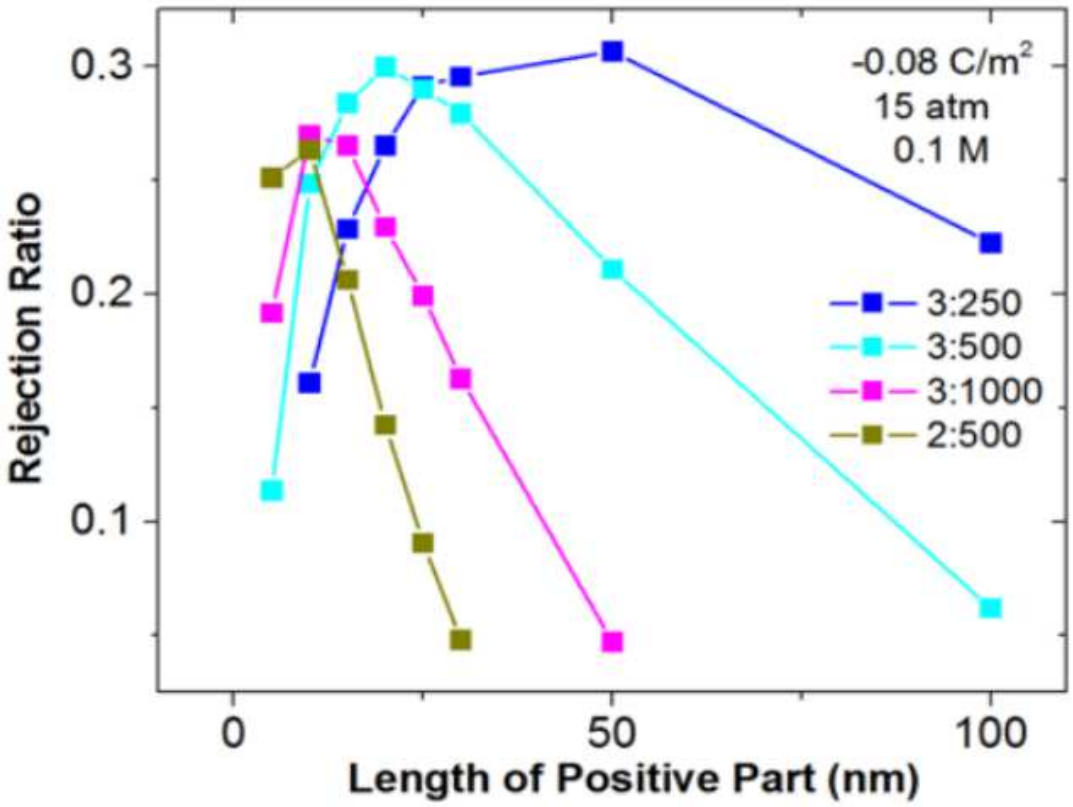

Figure 2.19. Rejection Ratio Dependence on Positive Effective Tip Length. The effect of the length of the positively charged region on desalination in conical nanopores is shown. Rejection shown is for 100 mM concentration at 15 atm through conical nanopores of varying diameter. The figure legend shows openings of the tip and base, respectively in nm.

3. Chemical Etching of Kapton Multipore Membranes

Etching of Kapton Membranes

The polyimide Kapton 50HN, poly (4,4'-oxydiphenylene-pyromellitimide), was created in the 1960s by Dupont from the condensation of pyromellitic dianhydride and 4,4'-oxydiphenylamine [38]. A monomer of Kapton is displayed in Figure 3.1. Kapton is an ideal polymer material due to its high tensile strength, temperature tolerance, insolubility to organic solvents, and stability after radiation exposure. Importantly, it is dissolved in strong alkalis allowing nanopore etching by highly basic (pH < 11) sodium hypochlorite (NaClO) at moderate temperatures [39].

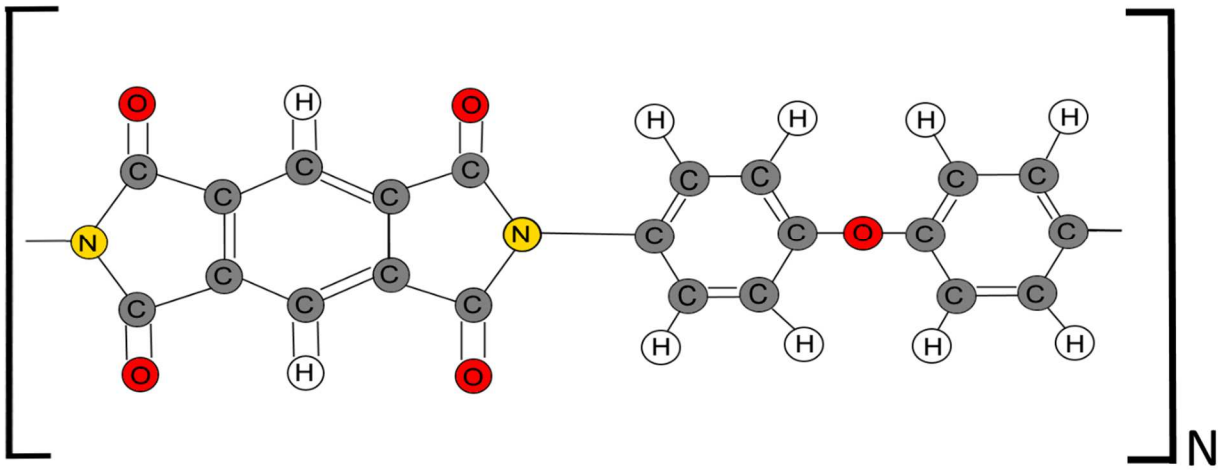

Figure 3.1. A Representative Monomer of Kapton.

The membranes we worked with were prepared by the track-etching technique consisting of two steps [40] [41] [42] [43] [44] [45]. In the first step, performed e.g. in the heavy ion accelerator in Darmstadt, Germany, ~12 μm thick films were irradiated with energetic heavy ions. The ions produced in the facility have energies of 11.4 MeV/u.

Each heavy ion produces one latent track, which in the next step of wet chemical etching leads to preparation of one pore. Experiments were performed with films irradiated with 10^8 ions/cm^2 or $2x10^8$ ions/cm^2. The beam of heavy ions is perpendicular to the membrane surface so that the resulting pores are parallel to each other.

Chemistry of etching

The second step for creating nanopores of desired size and geometry from the latent damage tracks in the Kapton films [46], uses alkaline hydrolysis of Kapton in NaClO. In this hydrolysis reaction, NaClO initially severs the Kapton monomer at the imide bond creating poly (amic acid) as illustrated in Figure 3.2b. Further hydrolysis reactions result in breakage of the imide bond and a return of the Kapton foil to its constituent monomers, pyrometallic acid and (chlorine substituted) aromatic diamine as shown in Figure 3.2c. Importantly, severing of the imide bond of the Kapton results in the formation of carboxyl groups upon the exposed surfaces of the etched foils. The surface of the Kapton foils thus acquire a negative surface charge at neutral and basic pH.

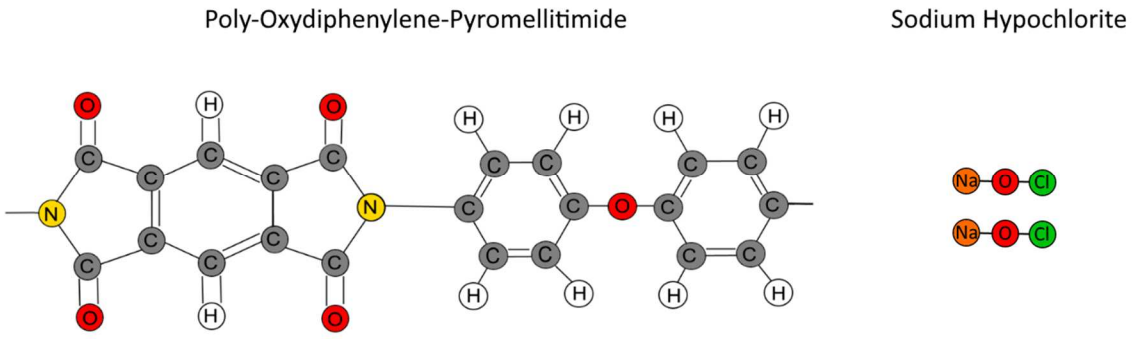

Figure 3.2a. Kapton etching by alkaline hydrolysis.

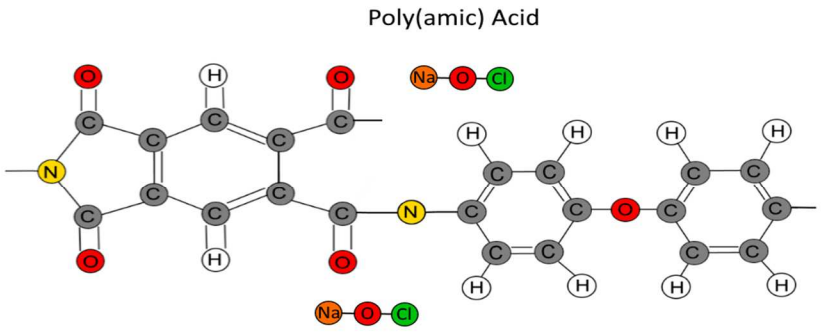

Figure 3.2b. A Broken Kapton Monomer. NaClO attacks the imide bond of the Kapton monomer.

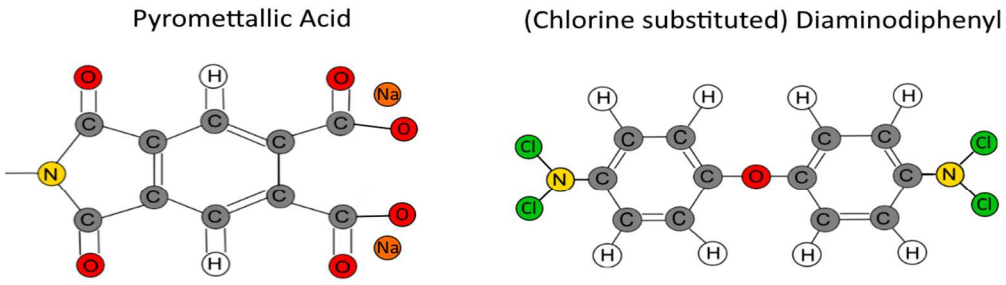

Figure 3.2c. Further hydrolysis of Kapton. The Kapton monomer returns to its constituent monomers after further etching.

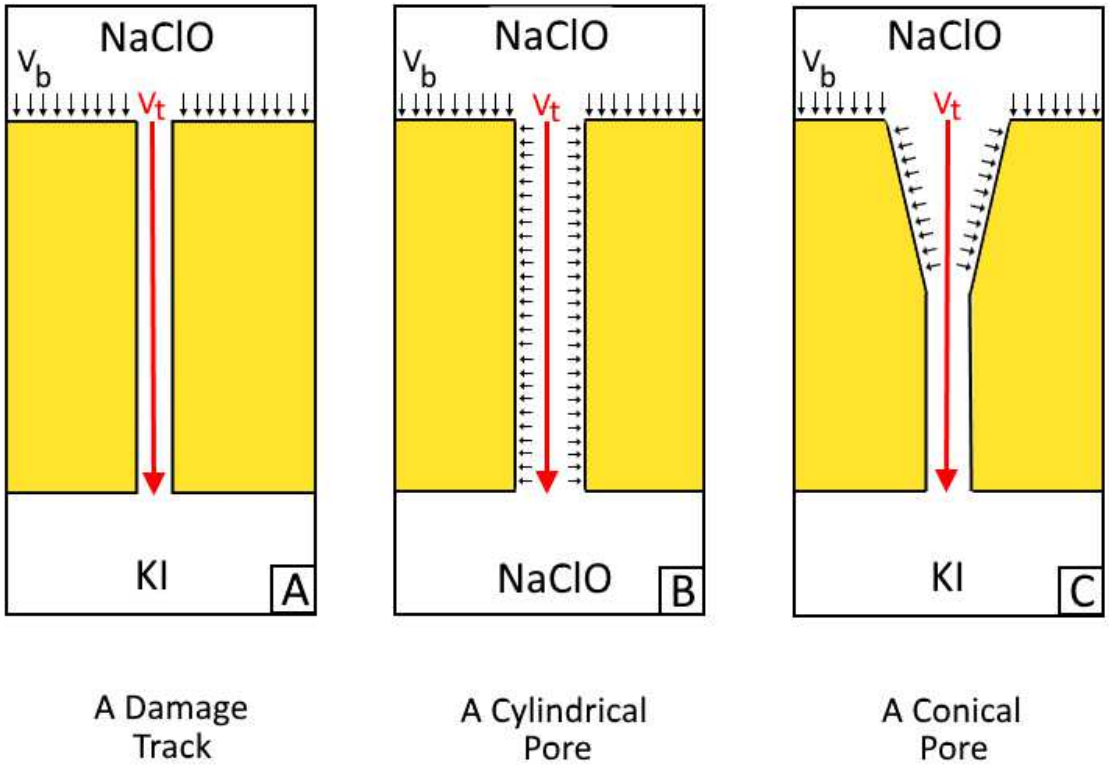

Figure 3.3. Etching of a Kapton Nanopore. A) Damage tracks in Kapton foils etched in NaClO. Pore geometry is governed by track etch rate, v_t, bulk etch rate, v_b, and presence of KI stopping solution for B) cylindrical pores and C) conical pores.

A schematic diagram of the etching process of Kapton foils is shown (Figure 3.3) for cylindrical and conical geometries. The resultant pore geometry is governed by the bulk etch rate of the etchant on the exposed surfaces of the foil, v_b, and the track etch rate, v_t, within the latent damage tracks [43]. The relationship between v_t and v_b determines the half opening angle β for conical shaped nanopores [40] and may be determined from

$$\beta = \arcsin\frac{v_b}{v_t} \tag{36}$$

Diverse geometries may be created through manipulation of the etching conditions, including conical, cylindrical, double conical, and conical with narrow stem.

The etching rates of Kapton by NaClO are primarily effected by the pH and temperature of the etchant. It has been demonstrated [ca] that etching Kapton with NaClO at pH < 7 produces no discernable pores in the foils. At 7≤pH<11 conical pores were formed. Additionally, the track etch rate has a linear dependence on pH, while the bulk etch rate depends exponentially on pH. Temperature dependence is the same for both track etch rate and bulk etch rate, which may be determined by eq. (37)

$$V_b = A\ exp\left(-\frac{E_b}{kT}\right) \tag{37}$$

Here A is a constant which depends upon the etchant and E_b is determined by the material etched. Siwy et al [26] experimentally determined a typical bulk etch rate of Kapton at 50^o C to be approximately 440 nm/hr. Following [42] we perform our etching processes with NaClO at 50^o. At this temperature etching times were nominally slower than studies performed at higher temperatures but there should be no discernable difference in current or rectification behavior of our nanopores.

Much of the physical phenomena we seek to exploit for ion rejection when maintaining high fluxes occurs due to the conical geometry of our nanopores. Thus, protection of the tip from excessive etching is paramount. Secondary measures to minimize etching rates at the tip side of the damage track include employment of a bath of stopping medium at this interface and application of an external potential across the pore. Once the etchant completely inundates the pore breakthrough occurs. At

breakthrough the stopping medium, in our case potassium iodide (KI), is able to enter the pore neutralizing etchant in the region near the tip. Prior to breakthrough a positive external voltage applied across the foil from tip to base will act to slow the etch rate within the damage track by minimizing the amount of etchant entering the pore. After breakthrough further etching on all internal and external surfaces is dependent only upon the bulk etch rate. Continued application of the potential as described after breakthrough will have only a negligible effect on total etch time.

4. Preparation of Kapton Nanopores and Experimental Methods

Kapton foils were obtained from the research facility GSI Helmholzzentrum fuer Schwerionenforschung, Darmstadt, Germany, and Belgian company IT4iP. The foils at GSI were irradiated with energetic uranium ions at the linear accelerator UNILAC. The films provided by IT4iP foils were irradiated with xenon ions. The damage-track density for GSI foils is $1x10^8$ pores/cm^2 and for IT4iP was $2x10^8$ pores/cm^2. Both foil types have a thickness of 12 microns.

Prior to beginning of the chemical wet etching process, foils were irradiated with 365 nm wavelength UV light for 60 minutes on each side within 24 hours of etching. Foils etched with this step omitted or reduced exposure times exhibited a longer etching period before breakthrough.

The wet etching process of Kapton was performed by placing the foils between two kel-F conductivity cells. The fluid cell volume of one kel-F cell was approximately 3 mL of liquid. The conductivity cell was placed in a heat bath of 3 L of distilled water carefully monitored at a constant 58^o C. It was found that due to the insulating properties of kel-F, when placed in the specified heat bath, solutions within the conductivity cells were maintained at 50^o C. Following previous work by [26], 50^o is our preferential temperature for wet-etching of Kapton by 13% sodium hypochlorite (NaClO).

After thermal equilibrium is reached between the heat bath and the conductivity cell, one side was filled with 1M potassium iodide (KI) heated to 50^o C. The KI solution is the stopping solution and NaClO is the etchant solution. The nanopore tip openings will

form at the membrane surface in contact with the stopping solution and this cell will be referred to as the 'tip.' NaClO is also heated to 50^{o} C and is placed in the opposite conductivity cell. It is on this side of the foil that the base of the nanopores will form through the membrane and hereafter the cell containing the etchant will be referred to as the 'base' side.

Platinum (Pt) electrodes and a Keithley 6487 picoammeter were employed to monitor currents in the conductivity cell throughout the etching process. Etching data was captured by a customized data acquisition program created in our lab with a sampling rate of 1 Hz. At the beginning of the etching process a positive 1 V potential was applied across the foil with the working electrode at the base side. Monitoring begins once the heated NaClO solution is placed in the base kel-f cell. During this time the etching current is observed to exhibit an initial negligible current followed by gradual current increase (Figure 4.1). We believe the current increase corresponds to subsequent pores being entirely etched through, i.e. the etchant has penetrated the whole track length. At this point the stopping solution has undergone a visual color-change from clear to amber due to the ion neutralization reaction between the KI and NaClO. The potential was shut-off once the etch current reached a value of 12-15 microamps.

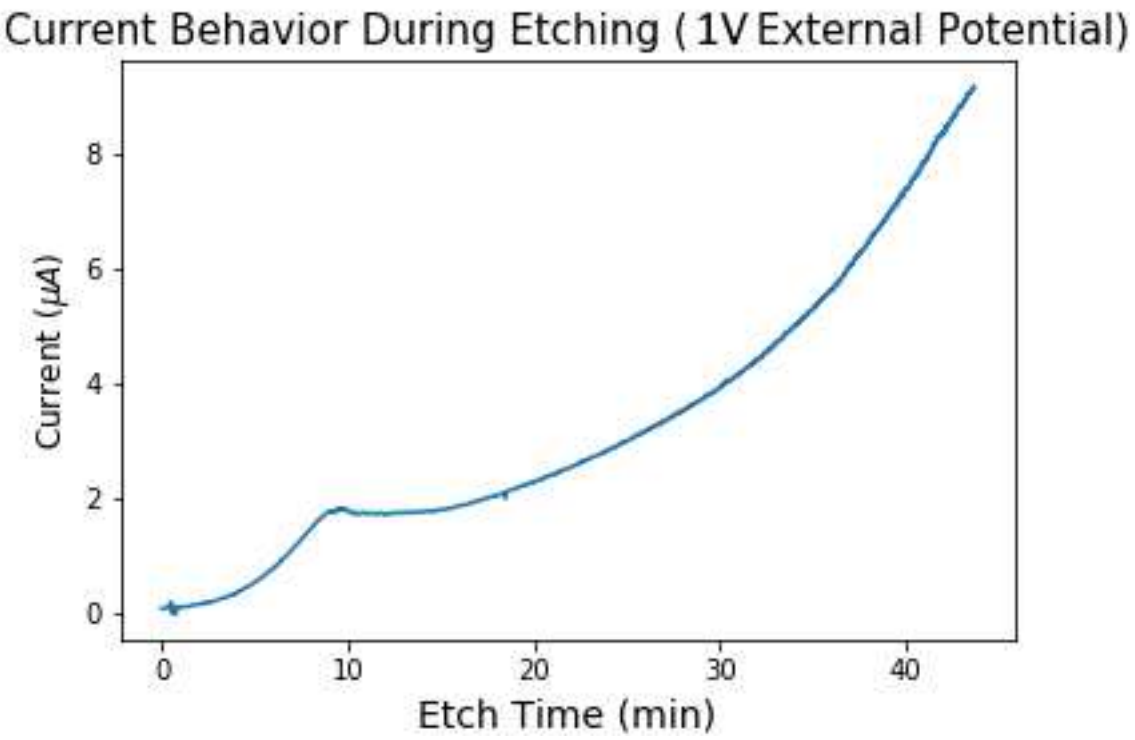

Figure 4.1. Initial Etching Current Behaviour of a Kapton Membrane. The etching current behavior of a Kapton membrane with a 1 V applied potential. Two Pt electrodes were used in the experiments, with the positively biased electrode at the etchant side of the foil (in the chamber filled with NaOCl).

Without an external applied potential, the etchant is allowed to diffuse through the latent track and once reaches the opposite side of the membrane, the opening is continuously being enlarged. Eventually, a plateau reached where the current maintains a constant value. When etching continued beyond this region, the current was observed to once more increase.

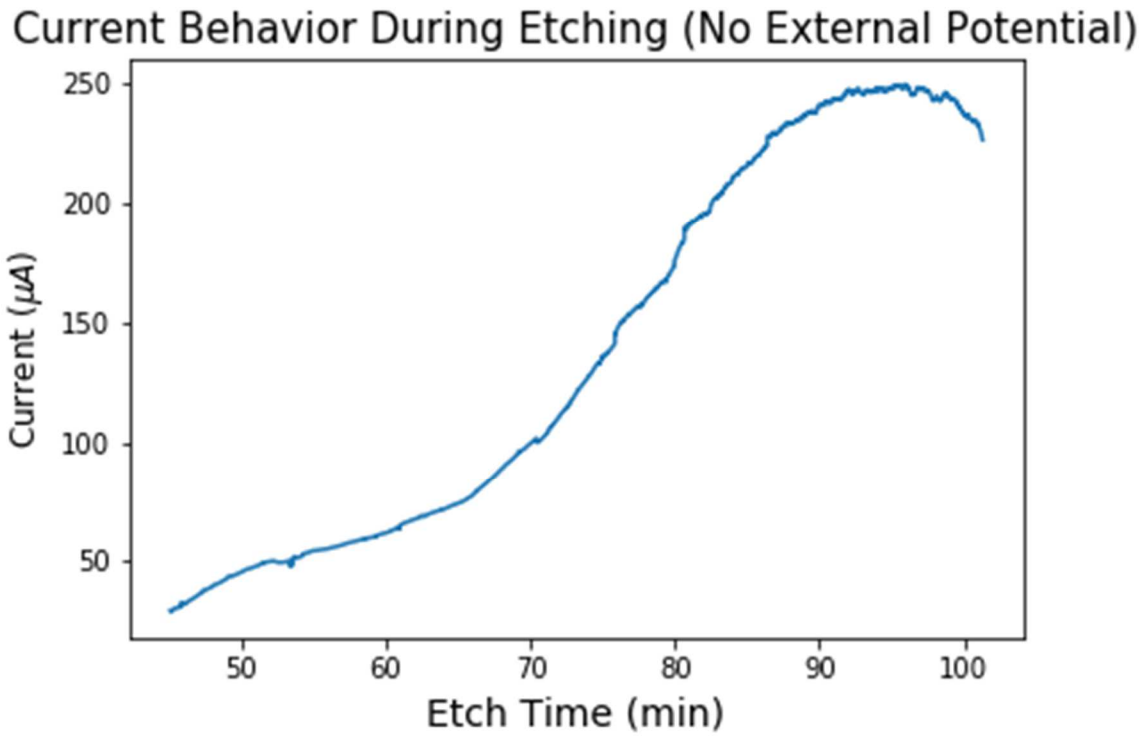

Figure 4.2. Diffusive Current Behavior of a Kapton Membrane During Etching. The current of a Kapton membrane was monitored with Pt electrodes during the second phase of the etching process. No external voltage was applied.

The etching process was terminated once current reached a plateau. Both solutions from both sides of the conductivity cell were removed and the membrane rinsed with fresh KI multiple times to neutralize any remaining etchant solution in the cells and pores. The membrane was then removed from the conductivity cell and rinsed with distilled water.

The etched Kapton membrane was subsequently characterized by measuring a current-voltage curve. The membranes were placed between clean conductivity cells sealed with parafilm. 100 mM potassium chloride (KCl), pH 8 (Tris buffer) was placed in both sides of the conductivity cell. A Keithley 6487 picoammeter/voltage source and Ag/AgCl electrodes were used to perform a potential sweep from negative to positive 1

V at 100 mV intervals per second. The working electrode was placed on the base side of the membrane. Example recordings are shown in Figure 4.3.

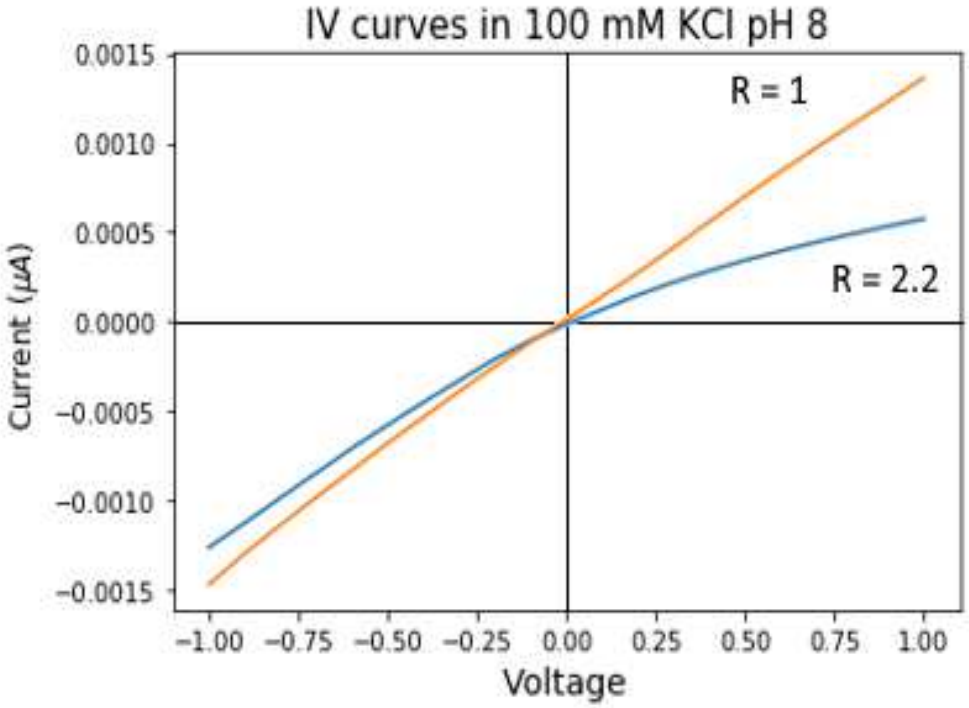

Figure 4.3. Kapton Membranes Characterized by Current-Voltage Curves. The Current-voltage curves of two independently prepared multipore Kapton membranes are shown with rectification ratio, R. Rectification is calculated as a ratio of currents at -1V and +1V respectively.

When recording current-voltage curve, we were especially interested in the presence of ion current rectification, reported before for single nanopores in Kapton and other materials. Presence of ion current rectification is indicative of nano-scale opening of the pores. Rectification, R, is calculated as a ratio of currents in -1V and +1V:

$$R = \left|\frac{I(-V)}{I(V)}\right| \tag{38}$$

Figure 4.3 shows two example membranes, one which rectifies current and one which does not.

Flow rates and desalination properties of each membrane were examined using an apparatus of two connected pressure cells. Unbuffered KCl at pH 5.5 and concentration of 100 mM was used as the feed solution placed on the side of the membrane with the larger opening. The tip side of the membrane was exposed to air. The pressure cell was suspended above a glass vial without contact. The vial was placed upon a balance with suitable precision for measuring mass changes in milligrams. Permeate which emerged at the tip side of the membrane dripped into the vial, and the changes in mass allowed us to calculate flow rate for each membrane (Figure 4.4).

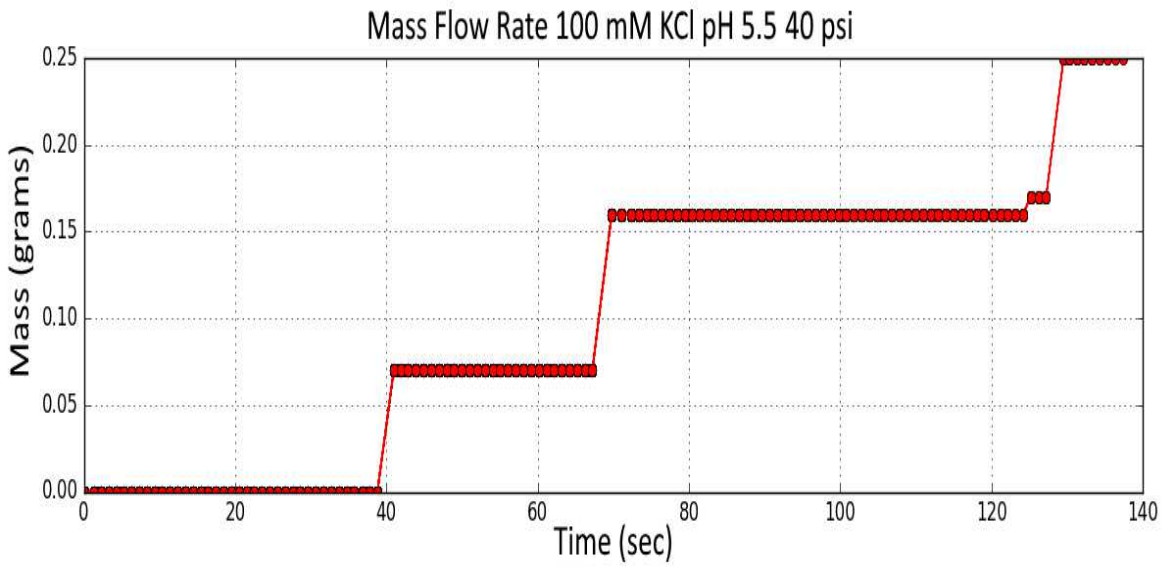

Figure 4.4. Flow Rate of a Multipore Kapton Membrane. The mass flow rate profile for a typical Kapton membrane is shown. 100 mM KCl, pH 5.5 was the feed solution. 40 psi pressure difference was applied. The calculated flow rate is 2 µL/sec.

Flow rates are computed from the average duration between permeate volume changes following the first observed change. Lag time prior to the first volume change was found to be highly variable for slow flow rates, whereas once flow began volume changes occurred more regularly. The flow rate of some membranes, in particular those with very low initial flow rates, were observed to abruptly cease. Whether this was due to bubbles formed by hydrophobicity at low pH, biofouling or scaling in the pores, concentration polarization, or some other mechanism, was not determined. More information on these possible causes may be found in Kucera [27].

The pressure cells had a volume of 3 mL. Only small volumes of permeate were collected in order to ensure the conductivity of the feed solution stayed nearly constant throughout the test. The desalination test was terminated after 500-600 µL of permeate entered the vial. The conductivity of the bulk solution, feed solution from the pressure cell after desalination, and permeate were tested using a (conductivity meter specifications). The conductivity probes must be submerged in at least 15 mL of solution for accurate readings, therefore 150 µL of each solution was diluted into 15 mL distilled water (conductivity 50 µS/cm). Samples were allowed to rest for fifteen minutes in order to reach thermal equilibrium with other samples and the testing environment. Multiple conductivity measurements, normalized to conductivity values at 25^{o} C, were taken to ensure accuracy. Desalination rates were reported as the percentage difference between the feed conductivity, C_F, and permeate conductivity, C_P as given in eq. (35).

$$R = \frac{C_F - C_P}{C_F} \tag{35}$$

Conductivity of the bulk feed was measured to maintain quality control.

Additional membranes were then selected for modification in .05 M spermine and .05 M EDC, (1-Ethyl-3-(3-dimethylaminopropyl)carbodiimide), solution. The basic modification solution is distilled water maintained at pH 5.5 by commercial buffers. A portion of this solution was modified by addition of .05 M spermine and readjusted to pH 5.5 by application of HCl and NaOH. The final modification solution was obtained by further addition of .05 M EDC.

The membrane was placed between two clean kel-F conductivity cells and sealed with parafilm. The base side cell was filled with the buffered KCl bulk solution. The tip side was filled with the .05 M spermine/EDC solution. The entire apparatus was sealed with parafilm and allowed to rest in a fumehood for the prescribed modification duration. After modification the cells were rinsed with distilled water and the membrane was removed.

Modified membranes were once again characterized by current-voltage curve by the same procedure given previously. Desalination tests were then preformed following identical procedures for unmodified membranes.

SEM Images of Kapton Membranes

Etched Kapton membranes were prepared for imaging by SEM. A 5 nm layer of gold is deposited by evaporation to provide the conductive layer required for imaging. Membranes were bisected in order to image tip and base regions. Figure 4.5 shows four images of a Kapton membrane.

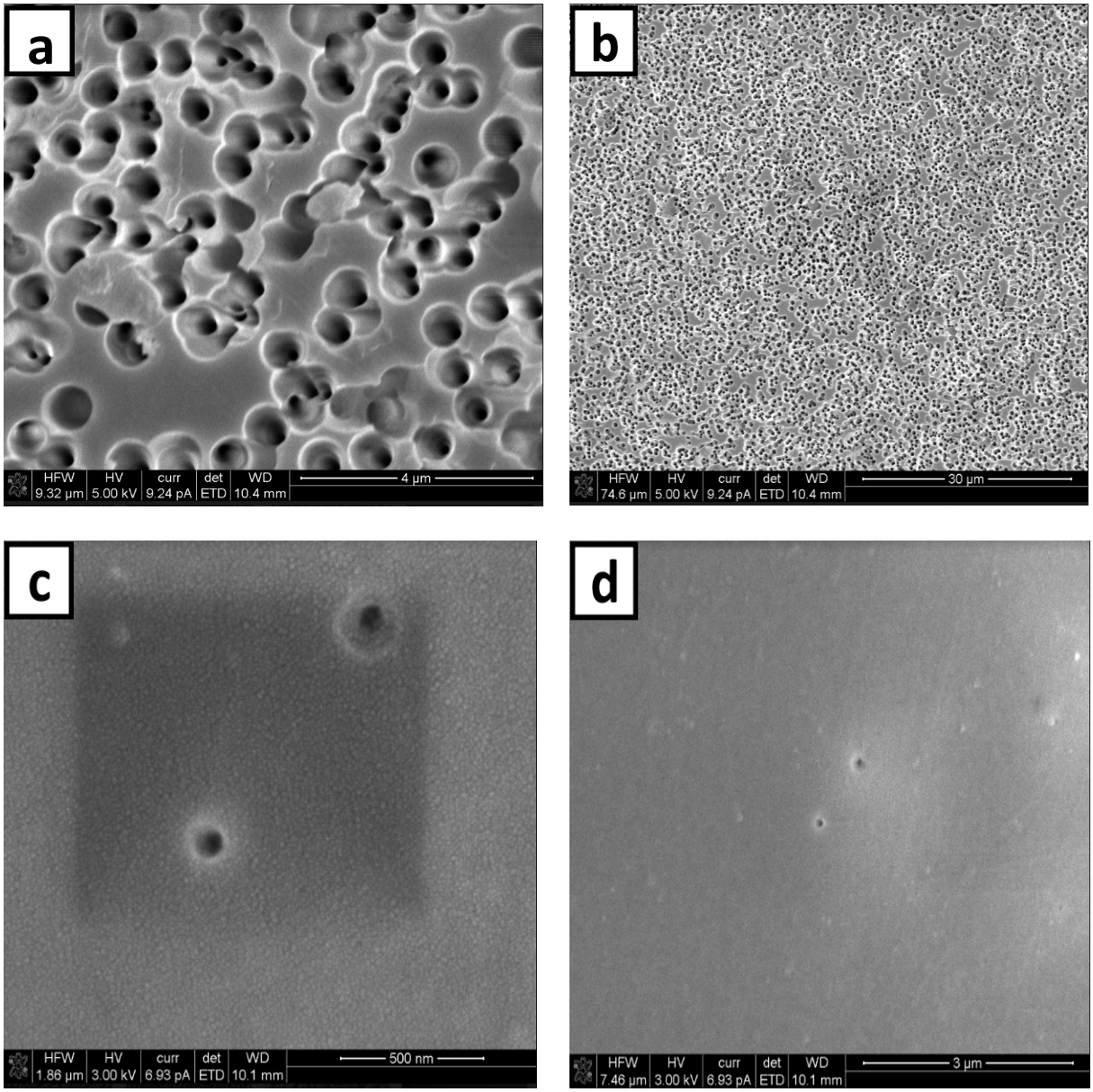

Figure 4.5. SEM Images of Tip and Base Openings of a Kapton Membrane. In a) base side diameters of approximately 400 nm diameter are shown. Conical geometry may be visually confirmed from this image. A wider view of the pore field is shown in b) confirming good homogeneity of pores. Tip diameters are shown in c) and d). Note the visible pore density on the tip side of the membrane is far less than that observed on the base side. This is due to resolution limitations of the SEM and possible coverage by Au deposition.

5. Data and Results

In initial experiments membranes were etched for a set duration of 120 minutes. This included a period of 60 minutes during which a 1 V positive potential was applied at the base side of the membranes followed by 60 minutes without an applied potential. Membranes prepared in this manner were found to have widely varying final etch currents, rectification ratios and behavior on current-voltage curves, and unpredictable flow rates. In order to gain better control over the desired final etch parameters of the membranes time dependent etching was exchanged in favor of terminating the etching process once a specified current value was reached.

Figure 5.1 shows an experiment where three Kapton membranes were prepared. Current was monitored using Pt electrodes and a Keithley 6487 picoammeter. We planned to use these membranes to confirm modification of surface charge in a further experiment, thus we desired that they contain pores small enough to exhibit rectification; the etching process was therefore ended when the etching current of each pore reached 115 μA. The etching time required for each membrane was 127 minutes, 88 minutes, and 117 minutes. Membranes were then characterized by current-voltage curves in 100 mM KCl at pH 8 to confirm rectification and determine rectification ratio.

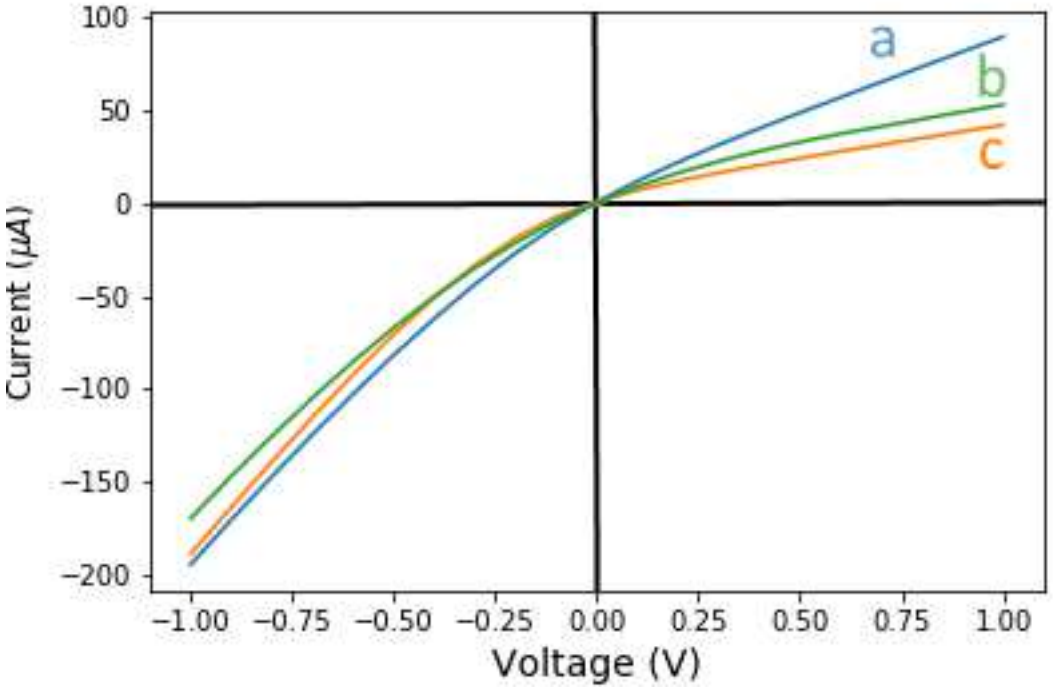

Figure 5.1. Current-Voltage Curves of Three Identically Prepared Kapton Nanopores. Etching was stopped when current reached 115 μA after a) 127 minutes, b) 88 minutes, c) 117 minutes. Data was taken in 100 mM KCl at pH8.

Although the etch times were vastly different for each membrane, rectification and current amplitudes of current-voltage curves were very similar across all three membranes. In the second experiment each of these membranes was then modified using 50 mM EDC and 50 mM spermine. The tip side of membrane ‘a’ was exposed to the modifying solution for 60 minutes, ‘b’ for 90 minutes, and ‘c’ for 120 minutes. After modification each membrane was characterized by a current-voltage curve as shown in Figure 5.2.

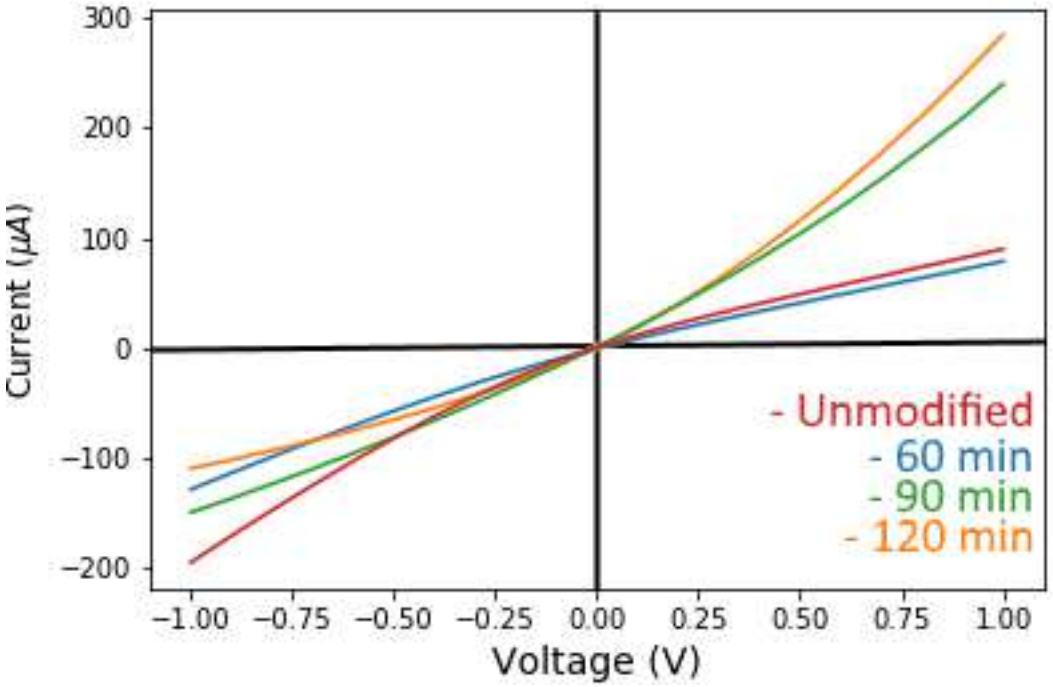

Figure 5.2. Current-Voltage Curves for Three Modified Kapton Membranes. Membranes were modified with 50 mM EDC and 50 mM spermine at the tip side of the membrane for the specified durations. The unmodified current-voltage curve of the membrane which was modified for 60 min is provided as a baseline. Curves were performed in 100 mM KCl at pH 8.

Figure 5.2 shows the dependence of ion current on the time of modification with spermine. The tip side of each membrane was exposed to the modifying solution for the specified duration. For reference the current-voltage curve of an unmodified membrane, specifically the membrane which was modified for 60 minutes, is shown. For the blue curve there was some decrease in current measured through the pore and no inversion of the previously seen rectification. The green and orange curves show complete inversion of the rectification. Also, currents are larger post modification but rectification ratios have decreased. We assume from these results that nearly the entire effective tip length has become positively charged for both the green and orange curves. From Figure 5.2 we surmised modification times of 80 mins were optimal for creating

nanopores with both positive and negative surface charged zones along the effective tip length.

The nanopores of the membranes shown in Figure 5.1 and Figure 5.2 were intentionally created small enough to ensure clear rectification would be shown to allow confirmation of the modification procedure. Consequently these membranes did not exhibit measureable flow during desalination experiments performed at the pressures available in our lab. Our next step was to create membranes which did exhibit flow and desalination, and then modify such membranes to compare salt rejection performance. Table 5.1 shows one such pore.

Surface Charge	Rectification Ratio	Pressure (PSI)	Flow Rate (μL/sec)	Desalination Percent
Unmodified	1.5	60	0	-
Unmodified	1.5	73	3	42
Diode	1.1	60	0	-
Diode	1.1	75	8	49

Table 5.1. Desalination of a Kapton Membrane Before and After Modification. Flow Rate and desalination of Kapton membrane prior to modification by 50 mM EDC and 50 mM spermine and after such modification is shown. The feed solution for the desalination experiment was 100 mM unbuffered KCl at pH 5.5. Note the membrane had no flow when subjected to a pressure gradient of 60 psi in either the diode or unmodified state.

Table 5.1 shows the desalination results for a Kapton membrane which was etched for 130 minutes. The etching current reached 188 μA when it was terminated. The membrane, initially unmodified, showed no flow for fifteen minutes at a pressure gradient of 60 psi. When the pressure was increased to 73 psi the membrane began to flow at 3 μL/sec. Using eq. (24) with this flowrate for the unmodified membrane, the

dynamic viscosity of water (0.001 Pa s), and pressure in pascals, nanopores on this membrane were found to have an average diameter of ~20 nm. The membrane was then modified for 80 min with 50 mM EDC and 50 mM spermine. Further desalination tests showed the now modified membrane still exhibited no flow at 60 psi and slightly improved desalination at 75 psi. The increase in flowrate after modification is not understood but may indicate the membrane was beginning to fail, as the membrane was completely compromised in the subsequent test.

Table 5.2 shows a representative sample of eight additional Kapton membranes which demonstrated desalination.

	Surface Charge	**Percent Rejection**
Membrane 1 – Kapton, 10^8 per cm^2	Diode	35% (100 mM), 60 psi
Membrane 2 – Kapton, 10^8 per cm^2	Diode	41% (100 mM), 60 psi
Membrane 3 – Kapton, $2*10^8$ per cm^2	Diode	50% (100 mM), 70 psi 65% (50 mM), 70 psi
Membrane 4 – Kapton, 10^8 per cm^2	Diode	55% (100 mM), 60 psi
Membrane 5 – Kapton, 10^8 per cm^2	Unmodified	16% (100 mM), 60 psi
Membrane 6 – Kapton, $2*10^8$ per cm^2	Unmodified	14% (100 mM), 60 psi
Membrane 7 – Kapton, $2*10^8$ per cm^2	Unmodified	14% (100 mM), 60 psi
Membrane 8 – Kapton, 10^8 per cm^2	Unmodified	17% (100 mM), 60 psi

Table 5.2. Desalination by Unmodified and Modified Kapton Membranes. Modified and Unmodified Kapton membranes which exhibited desalination are shown, including membranes with nanopore densities of $1*10^8$ and $2*10^8$ nanopores/cm^2.

Note, membrane 3 shows some evidence that desalination is improved as solute concentration is reduced. Also desalination rates are significantly higher for diode like modified pores. We believe these results show that membranes made from Kapton 50HN clearly exhibit desalination of 100 mM KCl at low pressures, and their parameters may be tailored by careful selection of the etching current at termination of the etching process. Desalination might be further improved by modifying the surface charge of the nanopores.

Experimental Difficulties, Further Considerations, and Future Work

The experiments and modeling presented in the thesis demonstrate that conically shaped nanopores with a bipolar surface charge pattern offer one solution for desalination of brackish water. In a single step experiment, salt rejection as high as ~55% was obtained from 100 mM KCl. A more complete desalination model is predicted via a multi-step process in which permeate from the first step becomes a feed solution for the subsequent step. An analysis of the salt rejection as a function of geometrical and chemical properties of nanopores is shown as well.

The main difficulties we encountered were related with the pores preparation. We believe that the experimental set-up used for etching would have to be improved. Since etching of Kapton occurs at elevated temperature one would have to assure a homogeneous temperature throughout the etching solution. A more homogeneous etching might also be achieved via exchange of the etchant during the etching process.

The issue of membrane support would have to be solved as well.

In future studies, we plan to examine the effect of concentration on desalination and experimentally verify the improvement of salt rejection with the decrease of the feed concentration.

6. Bibliography

[1] US Department of Agriculture, "*World Agricultural Supply and Demand Estimates"* (WASDE-575 – March 8, 2018), retrieved from usda.mannlib.cornell.edu, (2018).

[2] E. McLamb, "The Ecological Impact of the Industrial Revolution," retrieved from www.ecology.com, (2011)

[3] USAID, *"USAID Development Data Library,"* retrieved from www.usaid.gov (Dec 2017).

[4] FAO (Food and Agriculture Organization of the United Nations), *"Water withdrawal by sector, around 2010,"* AQUASTAT database (2016).

[5] B. Djebedjian, M. Mohamed, S. El-Sarraf and M. Rayan, "Evaluation of Desalination and Water Transport Costs (Case Study: Abu Soma Bay, Egypt)," *IWTC*, Sharm El-Sheikh, Egypt, (2005).

[6] NGWA (National Ground Water Association), "*Brackish Water Info Brief 2010*," retrieved from www.ngwa.org, (2010).

[7] A. Norris, R. Workman, Y. Fan, J. Eshelman, W. Timp, "Nanopore sequencing detects structural variants in cancer," *Cancer Biology & Therapy*, vol. 17 (3), pp. 246-253, (July 2015).

[8] S. Majd, E. C. Yusko, Y. N. Billeh, M. X. Macrae, J. Yang, and M. Mayer, "Applications of biological pores in nanomedicine, sensing, and nanoelectronics," *Current Opinions in Biotechnology*, vol. 21, no. 4, pp. 439–476, (2010).

[9] C. R. Crick, J. Y. Y. Sze, M. Rosillo-Lopez, C. G. Salzmann, and J. B. Edel, "Selectively Sized Graphene-Based Nanopores for in Situ Single Molecule Sensing," *ACS Applied Materials and Interfaces*, vol. 7, no. 32, pp. 18188–18194, (2015).

[10] M. Akeson, D. Branton, J.J. Kasianowicz, E. Brandin, D. W. Deame, "Microsecond time-scale discrimination among polycytidylic acid, polyadenylic acid, and polyuridylic acid as homopolymers or as segments within single RNA molecules," *Biophysical Journal*, vol. 77 (6): pp. 3227–33. (December 1999).

[11] A. Mara, Z. Siwy, C. Trautmann, J. Wan, and F. Kramme, "An Asymmetric Polymer Nanopore for Single Molecule Detection," *Nano Letters*, vol. 4, no. 3, pp. 497-501, (2004)

[12] M. Kolmogorov, E. Kennedy, Z. Dong, G. Timp, and P. Pevzner, "Single-Molecule Protein Identification by Sub-Nanopore Sensors*," PLOS Computational Biology*, vol. 13(5), (May 2017).

[13] W. Sparreboom, A. van den Berg, J. C. T. Eijkel, "Principles and Applications of Nanofluidic Transport," *Nature Nanotechnology*, vol. 4, pp. 713−720, (2009).

[14] Cervera J., Schiedt B., Neumann R., Mafe S. and Ramirez P., "Ionic conduction, rectification, and selectivity in single conical nanopores," *Journal of Chem*ical Physics, vol. 124, 104706 (2006)

[15] Z. Siwy, "Ion-Current Rectification in Nanopores and Nanotubes with Broken Symmetry," *Advanced Functional Materials,* vol. 16 pp.735–746, (2006).

[16] E. Kalman, "Controlling Ionic Transport for Device Design in Synthetic Nanopores," *Ph.D Dissertation*, University of California, Irvine, CA (2010).

[17] R. B. Schoch, J. Han, and P. Renaud, "Transport Phenomena in Nanofluidics," *Reveiws Modern Physics*, vol. 80, no. 3, pp. 839–883, 92008)

[18] H. Harned and D. French, 'A Conductance Method for the Diffusion Coefficients of Electrolytes,' *Annals of the New York Academy of Sciences*, vol 46 (5), (Dec 2006).

[19] H. Daiguji, P. Yang, and A. Majumdar, "Ion Transport in Nanofluidic Channels," *Nano Letters*, vol. 4, no. 1, pp. 137–142, (2004).

[20] D. Grahame, "The Electrical Double Layer and the Theory of Electrocapillarity,"*Chemical Reviews, vol. 41* (3), pp. 441-501 (1947**).**

[21] R. F. Probstein, *Physiochemical Hydrodynamics: An Introduction, 2nd Edition*, John Wiley and Sons, Inc., New York, NY (1994)

[22] A. Szymczyk, H. Zhu, B. Balannec, “Ion Rejection Properties of Nanofilteration Membranes with Inhomogenous Charge Distributions,” *Journal of Physical Chemistry B*, vol. 114, pp. 10143–10150, (2010).

[23] S. Qian and Y. Ai, *Electrokinetic Particle Transport in Micro-/Nanofluidics: Direct Numerical Simulation Analysis,* CRC Press, Boca Raton, FL, (2012).

[24] a Santafé-Moros, “Nanofiltration Modeling Based on the Extended Nernst-Planck Equation under Different Physical Modes,” *Proceedings of COMSOL Conference 2008 Handbook*, vol. 274, no. 2005, (2008).

[25] P. Apel, P. Ramirez, I. Blonskaya, O. Orelovitch, and B. Sartowska, ‘Accurate Characterization of Single Track-Etched Conical Nanopores,’ *Physical Chemistry Chemical Physics*, vol. 16, pp. 15214-15223 (2014)

[26] Z. Siwy, D. Dobri, R. Nuemann, C. Trautmann, and K. Voss, “Method of Producing Nanostructures in Membranes, and Asymmetrical Membrane,” US Record of Invention Disclosure, (2003).

[27] Kucera, J, *Reverse Osmosis: Industrial Applications and Processes*, Scrivener, Salem, MA (2010).

[28] U. Merten, *Desalination by Reverse Osmosis,* M.I.T. Press, Cambridge, MA (1966)

[29] T.-M. Chang and L. X. Dang, “Detailed Study of Potassium Solvation Using Molecular Dynamics Techniques,” *Journal of Physical Chemistry B*, vol. 103, no. 22, pp. 4714–4720, (1999).

[30] S. J. Stuart and B. J. Berne, “Effects of polarizability on the hydration of the chloride ion,” *Journal of Physical Chemistry*, vol. 100, no. 29, pp. 11934–11943, (1996).

[31] A. Yaroshchuk, Y. Boiko, and A. Makovetskiy, “Ion-rejection, Electrokinetic and Electrochemical Properties of a Nanoporous Track-Etched Membrane and Their Interpretation by Means of Space Charge Model,” *Langmuir*, vol. 25, no. 16, pp. 9605– 9614, (2009).

[32] M. Ali, B. Schiedt, K. Healy, R. Neumann, W. Ensinger, “Modifyong the Surface Tracj-Etched Conical Nanopores in Polyimide,” *Nanotechnology*, vol.19, no. 8, (2008)

[33] T. Tsuru, S. Nakao, S. Kimura, “Ion Seperation by Bipolar Membranes in Reverse Osmosis,” *Journal of Membrane Science*, vol. 108, pp. 269-278, (1995)

[34] I. Vlassiouk and Z. Siwy, “Nanofluidoc Diode,” Nano Letters, vol. 7, no. 3, pp. 552-556, (2007).

[35] Z. Siwy, Y. Qui, C. Yang, and J. Boyd, “Desalination Beyond Debye Screening Length Using Highly Charged Membranes with Asymmetric Nanopores.” US Record of Invention Disclosure, (2017).

[36] M. Huysmans and A. DassArgues, “Review of the use of Péclet numbers to determine the relative importance of advection and diffusion in low permeability environments,” Hydrogeology Journal, vol. 13(5-6), pp 895–904, (Oct 2005).

[37] S. Qian, Y. Ai, *“Electrokinetic Particle Transport in Micro-/Nanoflidics,”* CRC Press, Boca Raton, FL (2012).

[38] Dupont, “*DEC Kapton Summary of Properties*,” retrieved from www.dupont.com, (2017).

[39] C. Trautmann, W. Bruchle, R. Spohr, J. Vetter, and N. Angert, “Pore Geometry of Etched Ion Tracks in Polyimide,” *Nuclear Instruments and Methods in Physics Research B*, vol 111, pp. 70-74, (Sept. 1995)

[40] R. L. Fleischer, P. B. Price and R. M. Walker, *Nuclear Tracks in Solids*, University of California Press, Berkeley, CA, (1975).

[41] R. Spohr, “Status of Ion Track Technology—Prospects of Single Tracks,” *Radiation Measures*, vol. 40 (2-6) , pp. 191-202, (2005)

[42] Z. Siwy, P. Apel, D. Baur, D. Dobrev, Y. Korchev, R. Nuemann, R. Spohr, C. Trautmann, K. Voss, “Preparation of Synethetic Nanopores with Transport Analogous to Biological Channels,” *Surface Science*, vol. 532-535, pp. 1061-1066, (July 2003).

[43] C. Trautmann, W. Bruchle, R. Spohr, J. Vetter, and N. Angert, “Pore Geometry of Etched Ion Tracks in Polyimide,” Nuclear Instruments and Methods in Physics Research B, vol 111, pp. 70-74, (Sept. 1995)

[44] E. C. H. Silk and R. S. Barnes, “Examination of fission fragment tracks with an electron microscope,” *Philisophical Mag*azine, vol. 4, no. 44, pp. 970–972, (1959).

[45] R. L. Fleischer, P. B. Price, and R. M. Walker, “Track Registration in Various Solid-State Nuclear Track Detectors,” *Physical Reviews*, vol. 133, no. 5A, pp. A1443–A1450, (1964).

[46] Z. Siwy, P. Apel, D. Baur, D. Dobrev, Y. Korchev, R. Nuemann, R. Spohr, C. Trautmann, K. Voss, “Preparation of Synethetic Nanopores with Transport Analogous to Biological Channels,” *Surface Science*, vol. 532-535, pp. 1061-1066, (July 2003).